



Negative curvature fibers

CHENGLI WEI,¹  R. JOSEPH WEIBLEN,²  CURTIS R. MENYUK,² 
AND JONATHAN HU^{1,*} 

¹Department of Electrical and Computer Engineering, Baylor University, One Bear Place #97356, Waco, Texas 76798, USA

²Department of Computer Science and Electrical Engineering, University of Maryland Baltimore County, 5200 Westland Blvd., Baltimore, Maryland 21227, USA

*Corresponding author: jonathan_hu@baylor.edu

Received September 6, 2016; revised July 27, 2017; accepted July 28, 2017; published September 1, 2017 (Doc. ID 273269)

We describe the history, guiding mechanism, recent advances, applications, and future prospects for hollow-core negative curvature fibers. We first review one-dimensional slab waveguides, two-dimensional annular core fibers, and negative curvature tube lattice fibers to illustrate the inhibited coupling guiding mechanism. Antiresonance in the glass at the core boundary and a wavenumber mismatch between the core and cladding modes inhibit coupling between the modes and have led to remarkably low loss in negative curvature fibers. We also summarize recent advances in negative curvature fibers that improve the performance of the fibers, including negative curvature that increases confinement, gaps between tubes that increase confinement and bandwidth, additional tubes that decrease mode coupling, tube structures that suppress higher-order modes, nested tubes that increase guidance, and tube parameters that decrease bend loss. Recent applications of negative curvature fibers are also presented, including mid-infrared fiber lasers, micromachining, and surgical procedures. At the end, we discuss the future prospects for negative curvature fibers. © 2017 Optical Society of America

OCIS codes: (060.2280) Fiber design and fabrication; (060.2400) Fiber properties; (060.5295) Photonic crystal fibers
<https://doi.org/10.1364/AOP.9.000504>

1. Introduction	506
2. Guidance Mechanism	509
2.1. Antiresonant Reflection	510
2.1a. Slab Waveguide	510
2.1b. Annular Core Fiber	512
2.1c. Negative Curvature Fiber.	514
2.2. Inhibited Coupling	517
2.2a. Slab Waveguide	518
2.2b. Negative Curvature Fiber.	521
2.3. Comparison of the Guiding Mechanisms in Photonic Bandgap and Negative Curvature Fibers.	525
3. Recent Advances in Negative Curvature Fibers	526
3.1. Negative Curvature that Increases Confinement	526

3.2. Gap Between Tubes that Increase Confinement and Bandwidth.	528
3.3. Additional Tubes that Decrease Mode Coupling	529
3.4. Tube Structures that Suppress Higher-Order Modes.	531
3.5. Nested Tubes that Increase Guidance	533
3.6. Tube Parameters that Decrease Bend Loss.	535
4. Applications	537
4.1. Mid-IR Fiber Lasers.	537
4.2. Micromachining	539
4.3. Surgical Procedures	540
5. Future Prospects	541
6. Summary	544
Funding	545
Acknowledgment.	545
References	545

Negative curvature fibers

CHENGLI WEI, R. JOSEPH WEIBLEN, CURTIS R. MENYUK, AND JONATHAN HU

1. INTRODUCTION

Conventional step-index optical fibers have a higher-index material in the center and a lower-index material in the cladding in order to guide light by total internal reflection. Their guided modes have an effective index that is between the refractive indices of the core and cladding regions. The first microstructured optical fiber was fabricated in 1974 and consisted of a small-diameter rod supported on a thin plate in the center of a larger-diameter protective tube [1]. Research on periodic optical structures has grown rapidly [2] since photonic crystals were introduced in 1987 [3,4]. The first photonic crystal fiber (PCF) was demonstrated in 1996 [5,6]. It had a solid core with hexagonally spaced air holes along the entire length of the fiber with one missing defect hole that confined light in the central core [6,7]. In photonic crystal fibers of this type, there are one or more defect holes missing in the center, and these defects form the central core. The holey cladding forms an effective low-index material and confines the light. The effective index of the cladding is determined by the fundamental space-filling mode [7] and can be calculated using the tight binding model [8–11]. The confinement mechanism is still effectively the same as in conventional step-index fibers that use total internal reflection. Because of the flexibility of fiber design that includes air holes in the fiber, PCFs can have attractive properties, such as higher nonlinearity, endlessly single-mode transmission, tunable dispersion, and high birefringence [7,12–15].

In the late 1970s, a cylindrical Bragg waveguide, which consists of alternating rings of high- and low-refractive-index materials, was proposed. This waveguide uses a bandgap or a forbidden gap to confine the light in the central core with a low refractive index [16,17]. A bandgap implies that certain frequencies cannot propagate. If the light frequency is in the frequency range of the bandgap, the periodic cladding structure can confine the light in the central air core [13,14,18]. In addition, the effective index of the fundamental core mode will reside in the range of the bandgap [13,14,18]. In the late 1990s, hollow-core photonic bandgap fibers using a two-dimensional periodic cladding structure with an air core in the center attracted a large amount of interest due to their potential to realize optical properties that are not possible in conventional fibers [19,20]. The hollow-core photonic bandgap fibers can overcome some of the fundamental limitations of conventional step-index fibers and can in theory lead to reduced transmission loss, lower nonlinearity, and a higher damage threshold [18,21–23]. The central core, which confines the light, can be filled with gases or other materials, leading to long light–matter interaction lengths [18,24–26]. Later, kagome fibers were also developed to obtain low-loss transmission in an air core [27–30].

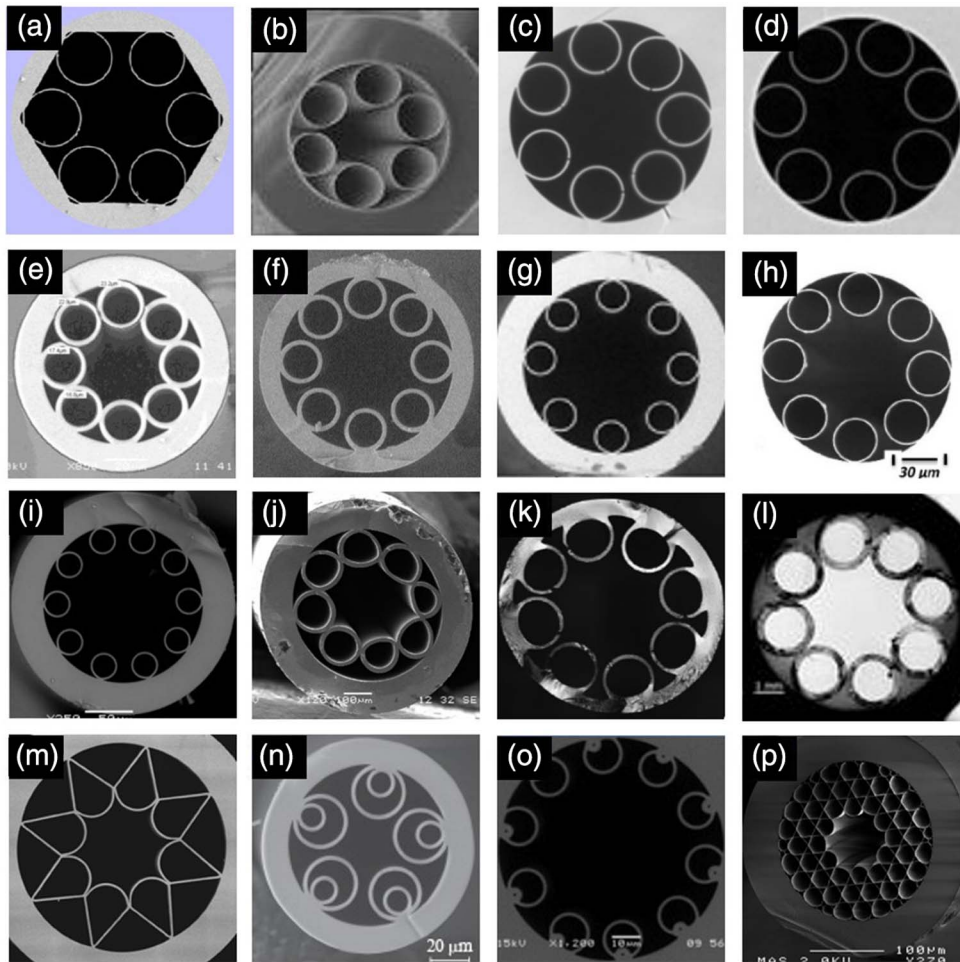
Besides the periodic cladding structure, antiresonant reflection can also confine light in the region with a low refractive index. It was first studied and experimentally realized in a one-dimensional slab waveguide in 1986 [31,32]. Two-dimensional structures with light transmission in a low-index core that use the same confinement mechanism have been studied [33–35]. Antiresonant reflective structures have been used to design the inner core boundary of photonic crystal fibers that have different cladding structures. These include kagome fibers, square-lattice hollow-core fibers,

and bandgap fibers [28,29,36–43]. By tuning the thickness of the core boundary, the antiresonant structure can also be used to minimize the field intensity at the glass and air interface [43–45].

Research on antiresonance and kagome fibers finally led to negative curvature fibers with a cladding that consists of one ring of tubes, taking advantage of both the simple cladding structure and the negative curvature of the core boundary [46–53]. In a negative curvature fiber, the surface normal vector of the core boundary is oppositely directed from a radial unit vector [36,47,54]. The negative curvature inhibits coupling between the fundamental core mode and the cladding modes. The cladding modes are modes that reside primarily inside the tubes, in the glass, or in the interstices between the tubes and the outer glass ring. Antiresonance is necessary to inhibit coupling between core and cladding modes in negative curvature fibers, but it is not sufficient. A combination of antiresonance in the glass at the core boundary and a wavenumber mismatch between the core and the cladding modes inhibits coupling between the modes and has led to remarkably low loss. By taking advantage of inhibited coupling, silica negative curvature fibers have been demonstrated with low transmission loss of the order of 10 dB/km [36,49–52,55–60]. Lower losses are relatively easier to achieve at larger core diameters [61]. Many analyses have been done on negative curvature fibers to study the effect on the fiber loss of the curvature of the core boundary, the number of cladding tubes, the thickness of the tubes, and the bend radius [42,62–71]. Enhancements of negative curvature fibers have also been suggested, including fibers with gaps between the cladding tubes [42,65–68] and fibers that include one or more nested tubes with additional reflecting surfaces [42,64,65]. Since no bandgap is used in negative curvature fibers, there is no requirement for a periodic cladding structure. The simplicity of the negative curvature structure opens up the possibility of fabricating fiber devices for mid-infrared (IR) applications using non-silica glasses [72–76], such as chalcogenide, since the development of hollow-core chalcogenide fibers has been hampered by fabrication difficulties [54,77,78].

Figure 1 shows scanning electron micrographs (SEMs) of hollow-core fibers with a negative curvature core–cladding interface. In particular, Figs. 1(a) and 1(c) show negative curvature fibers with six [79] and seven [57] cladding tubes to suppress higher-order core modes. Figure 1(b) shows a negative curvature fiber for Raman spectroscopy using ethanol [80]. Figure 1(d) shows a negative curvature fiber used for penalty-free 10G on–off keying data transmission through 100 m of fiber [59]. Figure 1(e) shows the fiber with one ring of touching tubes [48]. The loss can be further reduced by introducing a separation between the cladding tubes, as shown in Fig. 1(f) [50]. The mode content in a negative curvature fiber shown in Fig. 1(g) has been experimentally measured using spatially and spectrally resolved imaging [81]. A negative curvature fiber with a loss of 7.7 dB/km at 750 nm has been reported, as shown in Fig. 1(h) [56]. A negative curvature fiber with a larger separation between tubes corresponding to a small tube diameter has also been proposed for lower bend loss, as shown in Fig. 1(i) [68]. A 10.6 μm CO₂-laser delivery system has been fabricated with a chalcogenide negative curvature fiber, as shown in Fig. 1(j) [54]. Figure 1(k) shows a chalcogenide negative curvature fiber that was fabricated using extrusion [76]. Figure 1(l) shows a hollow-core negative curvature fiber made with polymethylmethacrylate (PMMA) tubes for terahertz (THz) spectrum transmission [82]. Figure 1(m) shows a hollow-core negative curvature fiber [49], which has been used for high-power applications in the mid-IR region [52,83]. Figures 1(n) and 1(o) show double antiresonant fibers with one small tube inside another tube [61,84]. Figure 1(p) shows a hypocycloid-shaped kagome fiber, in which curvature of the core boundary can be adjusted [36,85]. Table 1 displays the parameters of the fibers that are shown in Fig. 1.

Figure 1



Scanning electron micrographs (SEMs) of negative curvature fibers listed in Table 1. (a) Reprinted with permission from [79]. Copyright 2016 Optical Society of America. (b) Reprinted with permission from [80]. Copyright 2017 Optical Society of America. (c) Reprinted with permission from [57]. Copyright 2016 Optical Society of America. (d) © 2017 IEEE. Reprinted with permission from Hayes *et al.*, *J. Lightwave Technol.* **35**, 437–442 (2017) [59]. (e) Reprinted with permission from [48]. Copyright 2011 Optical Society of America. (f) Reprinted with permission from [50]. Copyright 2013 Optical Society of America. (g) Reprinted with permission from [81]. Copyright 2016 Optical Society of America. (h) Reprinted with permission from [56]. Copyright 2017 Optical Society of America. (i) Reprinted with permission from [68]. Copyright 2014 Optical Society of America. (j) Reprinted with permission from [54]. Copyright 2011 Optical Society of America. (k) Reprinted with permission from [76]. Copyright 2016 Optical Society of America. (l) Reprinted with permission from [82]. Copyright 2013 Optical Society of America. (m) Reprinted with permission from [49]. Copyright 2012 Optical Society of America. (n) Reprinted from Kosolapov *et al.*, *Quantum Electron.* **46**, 267–270 (2016) [61]. © IOP Publishing. Reproduced with permission. All rights reserved. (o) © 2015 IEEE. Reprinted with permission from Belardi, *J. Lightwave Technol.* **33**, 4497–4503 (2015) [84]. (p) Reprinted with permission from [36,85]. Copyright 2012 and 2013 Optical Society of America.

Table 1. Parameters in Negative Curvature Fibers

Figure	Fiber Material	Core Diameter	Wall Thickness	Loss	Wavelength	Ref.
(a)	Silica	30 μm	0.44 μm	0.18 dB/m	1.6 μm	[79]
(b)	Silica	32 μm	0.25 μm	100 dB/km	1.3 μm	[80]
(c)	Silica	30 μm	0.83 μm	30 dB/km	1.09 μm	[57]
(d)	Silica	40.2 μm	0.359 μm	25 dB/km	1.2 μm	[59]
(e)	Silica	27 μm	2.0 μm	<1 dB/m	1 μm	[48]
(f)	Silica	119 μm	6 μm	50 dB/km	3.39 μm	[50]
(g)	Silica	70 μm	1.2 μm	0.68 dB/m	1.5 μm	[81]
(h)	Silica	41 μm	0.545 μm	7.7 dB/km	0.75 μm	[56]
(i)	Silica	109 μm	2.4 μm	100 dB/km	3.1 μm	[68]
(j)	Chalcogenide	380 μm	18 μm	11 dB/m	10.6 μm	[54]
(k)	Chalcogenide	172 μm	7 μm	2.1 dB/m	10 μm	[76]
(l)	PMMA	3.24 mm	252 μm	0.16 dB/cm	362 μm	[82]
(m)	Silica	94 μm	2.66 μm	34 dB/km	3.05 μm	[49]
(n)	Silica	25 μm	2.3 μm	75 dB/km	1.85 μm	[61]
(o)	Silica	51 μm	1.27 μm	175 dB/km	0.48 μm	[84]
(p)	Silica	60 μm	1.4 μm	17 dB/km	1.064 μm	[36,85]

In the literature, negative curvature fibers are referred to as hollow or hollow-core antiresonant fibers [63,64,68,84,86–90], hypocycloid-shaped hollow-core photonic crystal fibers [36,37,47,85,91–96], inhibited coupling fibers [94,97–100], negative curvature fibers [50–54,62,66,67,69,77,101], revolver fibers [61,102–105], and tube lattice fibers [82,106–112]. Since all these fibers take advantage of negative curvature in the region surrounding the central core, we will refer to them collectively as negative curvature fibers, which are the focus of this review. Hollow-core fibers with straight membranes in the region surrounding the central core also use antiresonant reflection, which contributes to inhibited coupling [29,40,41,113–116]. However, they do not use negative curvature and are outside the scope of this review.

The rest of the paper is organized as follows: Section 2 describes the inhibited coupling guidance mechanism in one-dimensional slab waveguides, two-dimensional annular core fibers, and negative curvature fibers. The guidance mechanism, the transmission loss, and the mode properties have been studied separately in slab waveguides [31,32], annular core fibers [89,106,117], and negative curvature fibers [48–51]. Annular core fibers can be used to predict the effective indices of the modes in negative curvature fibers, although not the loss. Section 3 presents recent advances in the design of negative curvature fibers, including negative curvature that increases confinement, gaps between tubes that increase confinement and bandwidth, additional tubes that decrease mode coupling, tube structures that suppress higher-order modes, nested tubes that increase guidance, and tube parameters that decrease bend loss. Although negative curvature fibers are relatively new, recent advances have increased their usefulness for a large range of applications. Section 4 presents applications of negative curvature fibers, including mid-IR fiber lasers, micromachining, and surgical procedures. We also discuss future prospects for negative curvature fibers in Section 5. A summary is given in Section 6.

2. GUIDANCE MECHANISM

The guidance mechanism in negative curvature fibers is inhibited coupling between light that propagates in the fiber core and light that propagates in the glass, in the cladding tubes, or in the interstices between the cladding tubes and the glass wall. Antiresonance plays a critical role in inhibiting the coupling between light in the core and in other regions of the negative curvature fiber, although some wavenumber mismatch is always needed. In Subsection 2.1, we describe antiresonant reflection in one-dimensional slab waveguides, two-dimensional annular core fibers, and negative curvature fibers. In Subsection 2.2, we describe that a wavenumber mismatch

between the core and cladding modes will contribute to inhibited coupling. The combination of antiresonance and a wavenumber mismatch between the fundamental core and the cladding modes inhibits coupling between the modes. The inhibited coupling mechanism differs significantly from the guidance mechanism in photonic bandgap fibers. In Subsection 2.3, we compare these two guidance mechanisms. Throughout Section 2, we use a wavelength of $1.0\ \mu\text{m}$, a refractive index of 1.45 for silica glass, and a refractive index of 1.0 for air.

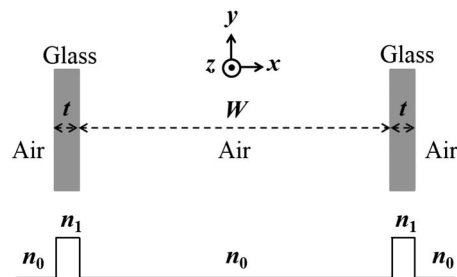
2.1. Antiresonant Reflection

We show simulation results with different structures that summarize simulations that have appeared in [48,89,106,118,119], to illustrate the antiresonant reflection mechanism, the transmission loss, and the mode properties. This subsection illustrates the important role of antiresonant reflection in guiding the light.

2.1a. Slab Waveguide

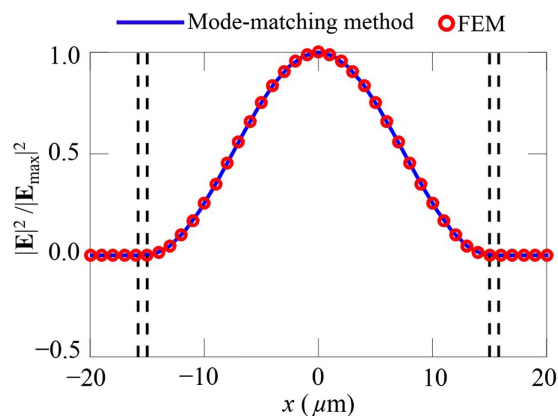
We first study the modes in a one-dimensional M -type slab waveguide. A schematic illustration of the refractive index profile of the M -type slab waveguide that extends infinitely in the y - and z -directions, is shown in Fig. 2. The gray regions represent glass. The white regions represent air. The normalized electric field intensity of the fundamental mode is shown in Fig. 3. The width of the air core is $30\ \mu\text{m}$,

Figure 2



Cross section and index profile of an M -type slab waveguide.

Figure 3

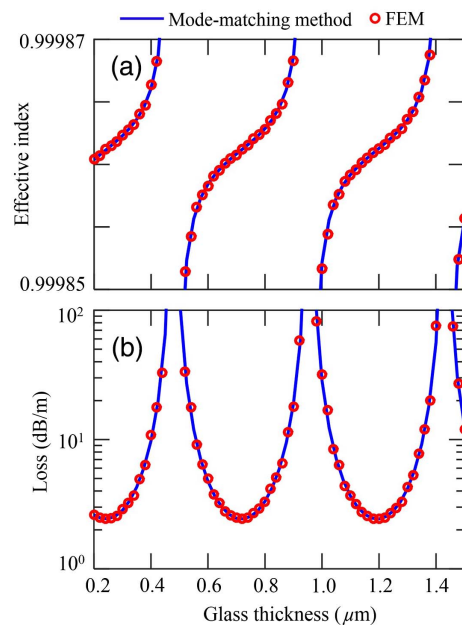


Normalized electric field intensity of the fundamental core mode in an M -type slab waveguide. The blue curve and red circles are the results from the mode-matching method and the FEM, respectively. The dashed lines indicate interfaces between air and glass.

and the glass thickness is $0.8 \mu\text{m}$. We calculate the effective index and leakage loss for the fundamental core mode in the M -type slab waveguide, with both the mode-matching method [120,121] and the finite-element method (FEM) [122,123], as shown in Fig. 4. The details of the mode-matching method and the FEM for the slab waveguide can be found in [120,123]. Both the mode-matching method and the FEM can give accurate predictions for the effective index and the loss in the M -type slab waveguide. It takes 2 s and 11 s on a desktop computer with a CPU speed of 3.4 GHz using the mode-matching method and the FEM, respectively, to find the effective index of the fundamental core mode in the M -type slab waveguide shown in Fig. 2. The mesh size and thickness of the absorbing layers must be verified for convergence when using the FEM, leading to additional computational cost. Given the complex effective index $n_{\text{comp}} = n_{\text{eff}} + in_{\text{imag}}$, which is what either method directly yields, the leakage loss is calculated as $\text{loss} = 40\pi n_{\text{imag}} / [\ln(10)\lambda]$, where λ is the wavelength [124,125]. The effective index equals the real part of the complex effective index. As the glass thickness increases from $0.2 \mu\text{m}$ to $1.5 \mu\text{m}$, there are three high-loss thicknesses of $0.48 \mu\text{m}$, $0.95 \mu\text{m}$, and $1.43 \mu\text{m}$, as shown in Fig. 4.

A schematic illustration of the reason for the high loss, which is due to a resonance condition, is shown in Fig. 5. For the core mode in the structure with a large core width where $W \gg \lambda$, the longitudinal wave vector, k_L , can be approximated by $n_0 k_0$, and the transverse wave vector, k_T , in the glass region, can be approximated by $k_0(n_1^2 - n_0^2)^{1/2}$. The parameter $k_0 = 2\pi/\lambda$ denotes the wave vector in the air. Then, the phase difference between the waves passing through the glass slab with and without additional reflections is $2tk_0(n_1^2 - n_0^2)^{1/2}$. The resonance condition that the phase difference is a multiple of 2π yields $t = m\lambda/[2(n_1^2 - n_0^2)^{1/2}]$, where m equals any positive integer [31–33]. The values of the thickness, t , corresponding to the resonances at $m = 1, 2,$ and 3 , are $0.48 \mu\text{m}$, $0.95 \mu\text{m}$, and $1.43 \mu\text{m}$, respectively, which correspond to the high-loss regions in Fig. 4(b). The minimum loss of 2.4 dB/m is the same in different

Figure 4



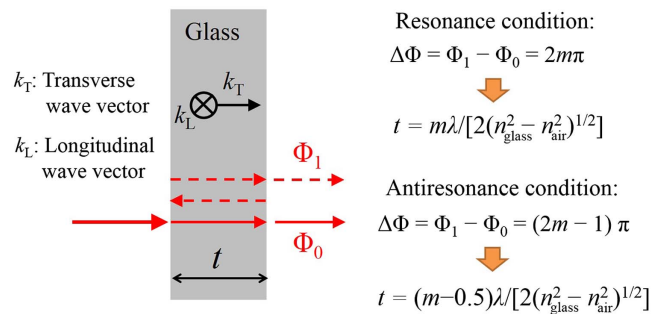
(a) Effective index and (b) leakage loss of the fundamental core mode as a function of glass layer thickness, t . The blue curves and red circles are the results from the mode-matching method and the FEM, respectively.

transmission bands in the M -type slab waveguide. We also show a contour plot of the leakage loss of the fundamental core mode as a function of the glass thickness and the air-core width in Fig. 6. There are three transmission bands, I, II, and III near the antiresonance condition, $t = (m - 0.5)\lambda/[2(n_1^2 - n_0^2)^{1/2}]$, where m equals any positive integer [33,126,127]. These transmission bands are between the high-loss regions corresponding to the resonance condition at glass thicknesses of 0.48 μm , 0.95 μm , and 1.43 μm . The resonance condition does not change with different widths of the air core. The leakage loss decreases as the width of the air core increases [42,111,128]. Note that the resonance condition and antiresonance condition can also be derived by using the conditions of minimum and maximum reflection, respectively, from the equations for multiple-beam fringes with a plane-parallel plate [129].

2.1b. Annular Core Fiber

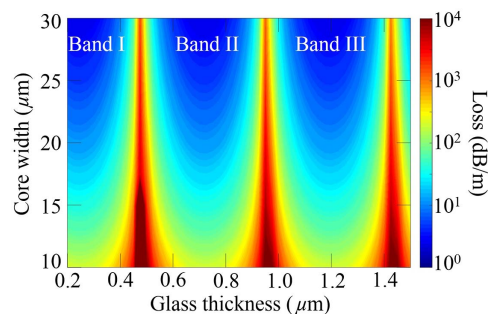
The cylindrical waveguide that corresponds most closely to the M -type slab is the annular core fiber, which has a high-index ring in the fiber geometry [130–132]. In Fig. 7, we show the cross section and the index profile along the radial direction of the annular core fiber. The gray regions represent the glass. The white regions represent the air. Annular core fibers with modes that exist in the glass ring have been extensively studied [130–132]. The effective index in this case is between the refractive indices of n_0 and n_1 . This subsection focuses on annular core fibers with modes that exist inside the central air core. These modes have an effective index that is less than either of the refractive indices n_0 or n_1 [89,106,117–119]. We find the core mode using the mode-matching method [130,133] and FEM [122,123].

Figure 5



Schematic illustration of the resonance and antiresonance conditions.

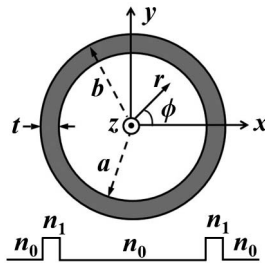
Figure 6



Leakage loss of the fundamental core mode in the M -type slab waveguide as a function of the glass thickness and the core width.

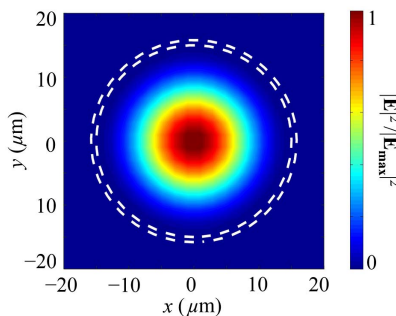
Figure 8 shows a contour plot of the normalized electric field intensity of the fundamental core mode in an annular core fiber with an air-core diameter of $30\ \mu\text{m}$ and a glass thickness of $0.8\ \mu\text{m}$. Figures 9(a) and 9(b) show the effective index and the leakage loss of the fundamental core mode as a function of glass thickness. The blue solid curves represent the results from the mode-matching method. The red circles represent results that are calculated using the FEM. Anisotropic perfectly matched layers (PMLs) are positioned outside the cladding in order to reduce the size of the simulation window [134]. It takes 7 s and 29 s on a desktop computer with a CPU speed of 3.4 GHz using the mode-matching method and the FEM, respectively, to find the effective index of the mode in the annular core fiber shown in Fig. 7. A longer time is required to use the FEM since a small mesh size is required in the model, especially in the thin glass regions. Also, convergence tests must be carried out on the mesh sizes in different regions of the fiber structure and on the thickness of the PML in order to obtain accurate results. While the mode-matching method runs more quickly, it can only be used in highly regular geometries like the annular core fiber, and cannot be used in irregular waveguide geometries, such as the negative curvature fibers that are shown in Fig. 1. We can see three high-loss regions at $0.48\ \mu\text{m}$, $0.95\ \mu\text{m}$, and $1.43\ \mu\text{m}$ in Fig. 9(b), which are consistent with the results shown in Fig. 4(b) for the *M*-type slab waveguide. The minimum loss of 23 dB/m is the same in different transmission bands in the annual core fiber. In Fig. 10, we also show a contour plot of the loss of the fundamental core mode as a function of the glass thickness and the core diameter. Low-loss antiresonant transmission bands exist between the high-loss regions corresponding to the resonance condition at the glass thicknesses of $0.48\ \mu\text{m}$, $0.95\ \mu\text{m}$, and $1.43\ \mu\text{m}$. The resonance condition does not

Figure 7



Cross section and index profile along the radial direction of an annular core fiber.

Figure 8



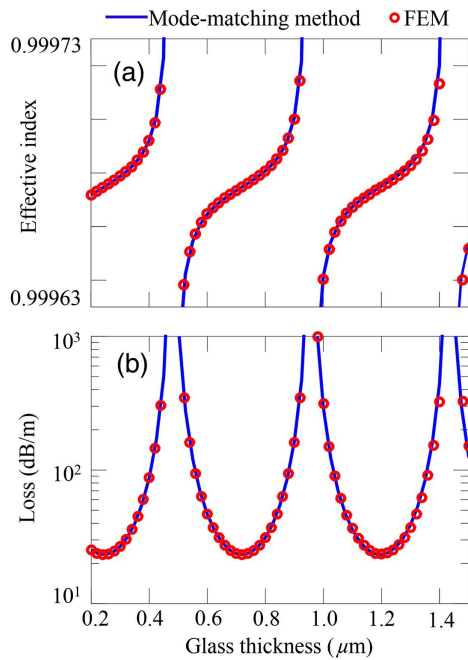
Contour plot of the normalized electric field intensity of the fundamental core mode in an annual core fiber. The white dashed lines indicate the boundaries of the glass ring.

change with different air-core diameters. The leakage loss decreases as the air-core diameter increases [42,111,128].

2.1c. Negative Curvature Fiber

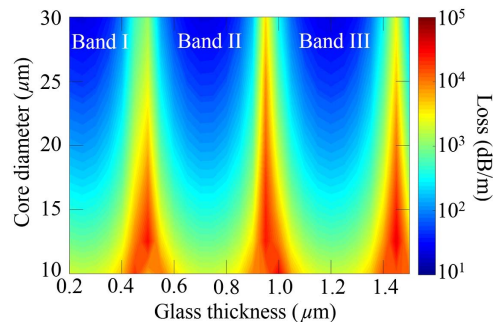
We now consider the fundamental core mode in a simple negative curvature fiber. The full fiber geometry is shown in Fig. 11. The gray regions represent glass, and the white regions represent air. We model a negative curvature fiber with eight cladding tubes. The thickness of the tube walls, t , the inner tube diameter, d_{tube} , the number of tubes, p , and the core diameter, D_{core} , are related by the expression $D_{\text{core}} = (d_{\text{tube}} + 2t) / \sin(\pi/p) - (d_{\text{tube}} + 2t)$ [57,69,126,127,135]. The normalized electric field intensity of the fundamental core mode with parameters

Figure 9



(a) Effective index and (b) leakage loss of the fundamental core mode as a function of glass thickness. The blue solid curves and red circles represent the results from the mode-matching method and the FEM, respectively.

Figure 10

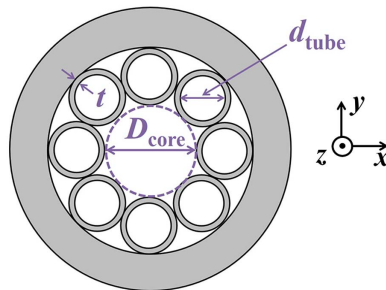


Leakage loss of the fundamental core mode in the annual core fiber as a function of the glass thickness and the core diameter.

$D_{\text{core}} = 30 \text{ }\mu\text{m}$ and $t = 0.8 \text{ }\mu\text{m}$, is shown in Fig. 12. Only a quarter of the geometry is used in modeling the hollow-core fiber in Fig. 11 because of the symmetry of the modes [124,136].

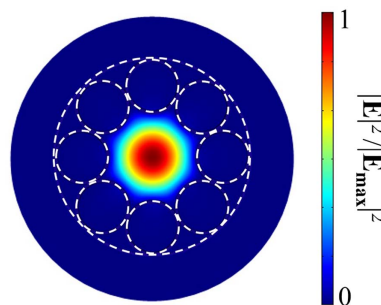
Figures 13(a) and 13(b) compare the effective index and leakage loss of the fundamental core mode as a function of glass thickness in the negative curvature fiber and in the annular core fiber. The results in the negative curvature fiber were obtained using the FEM, and the results in the annular core fiber were obtained using the mode-matching method. The core diameters of the annular core fiber and the negative curvature fiber are both $30 \text{ }\mu\text{m}$. In Fig. 13(a), the effective index of the fundamental core mode in the negative curvature fiber is larger than the effective index of the fundamental core mode in the annular core fiber by 3×10^{-5} . The reason is that the negative curvature boundary effectively increases the core diameter in the negative curvature fiber [69]. We next calculate the mode in the annular core fiber with a core diameter of $31.5 \text{ }\mu\text{m}$, which is increased by 5% to compensate for the effective increase in the core diameter that occurs in a negative curvature fiber. The corresponding results for the effective index and loss for an annular core fiber with a core diameter of $31.5 \text{ }\mu\text{m}$ are marked by the red circles in Fig. 13. With an empirical 5% increase in the core diameter, the effective indices of the core modes in the annular core fiber match the effective indices of the core modes in the negative curvature fiber when the glass thickness is in the antiresonant region in Fig. 13(a). In Fig. 13(b), the glass thicknesses corresponding to the resonance conditions or high-loss regions in the negative curvature fiber are slightly larger than the glass thicknesses in the annular core fiber. The reason is that the curvature effectively lowers the glass thickness [70]. The leakage loss decreases slightly when the core diameter increases from $30 \text{ }\mu\text{m}$ to $31.5 \text{ }\mu\text{m}$ in the

Figure 11



Full hollow-core negative curvature fiber geometry.

Figure 12

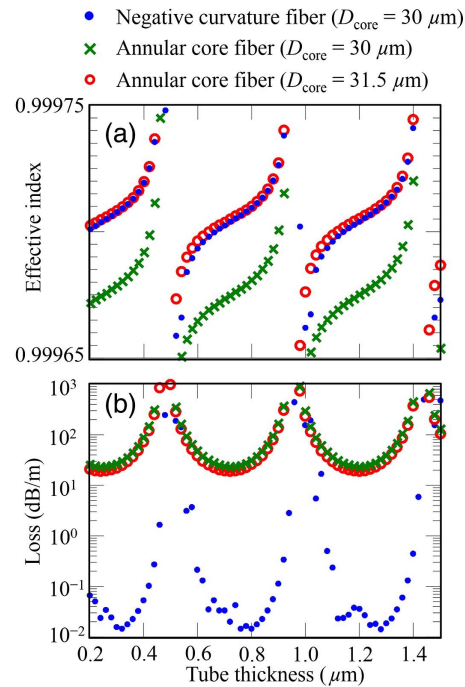


Normalized electric field intensity of the fundamental core mode in a negative curvature fiber. The white dashed curves indicate the boundaries of the glass.

annular core fiber. However, the leakage loss in the negative curvature fiber is lower than the leakage loss in the annular fiber by 3 orders of magnitude due to the negative curvature [36,63]. Since cladding tubes are touching, localized nodes are created, and glass modes exist in the localized node area [50]. Fluctuations of the leakage loss in the transmission bands are due to the mode field in the localized node area in negative curvature fibers [36].

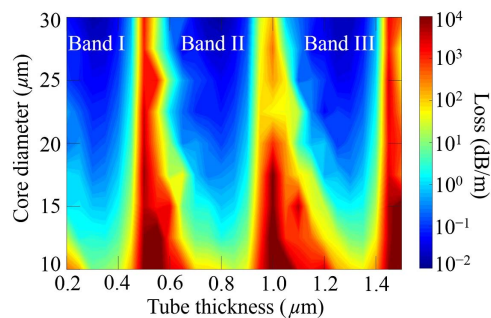
Figure 14 shows a contour plot of the leakage loss of the fundamental core mode as a function of the glass thickness and the core diameter in the negative curvature fiber.

Figure 13



(a) Effective index and (b) leakage loss of the fundamental core mode as a function of tube thickness. The blue dots, the green crosses, and the red circles represent the results in the negative curvature fiber with a core diameter of $30 \mu\text{m}$, the annular core fiber with a core diameter of $30 \mu\text{m}$, and the annular core fiber with a core diameter of $31.5 \mu\text{m}$, respectively.

Figure 14



Leakage loss of the fundamental core mode in the negative curvature fiber as a function of the tube thickness and the core diameter.

The three transmission bands are still visible between the high-loss regions, corresponding to the resonance conditions. The resonance condition does not change with different air-core diameters. The leakage loss decreases as the air-core diameter increases [42,111,128].

The same transmission bands are obtained in simulations with silica glass that include an imaginary refractive index of 9×10^{-8} , in accordance with the experimentally measured material loss [137]. The leakage loss increases by less than 5% compared with the previous simulation that did not include the imaginary part of the complex refractive index of the silica glass.

2.2. Inhibited Coupling

Antiresonant reflection impedes the penetration of light into the glass that surrounds the core, and is necessary to achieve the low loss that has been observed in negative curvature fibers. However, as the comparison between annular core and negative curvature fibers in Subsections 2.1b and 2.1c shows, it is not sufficient. More generally, the coupling between the core and cladding modes must be inhibited [36,56]. Inhibited coupling means that leakage of the core mode into the cladding is suppressed by a strong reduction in the coupling between the core mode and the cladding modes [36,56]. The coupling between the core and cladding modes is reduced by having a small spatial mode overlap and a mismatch of their wavenumbers or effective indices [36,56]. In order to effectively inhibit coupling, both conditions should be met. Antiresonance reduces the mode overlap. A smaller overlap reduces in turn the wavenumber mismatch that is needed to inhibit coupling, but some mismatch is always needed.

In this subsection, we first review inhibited coupling in a three-slab waveguide in which glass partitions separate an air-core slab from two surrounding air-cladding slabs. We then review inhibited coupling in the simple negative curvature fiber that we considered in Subsection 2.1c, although here we consider the effect of decreasing in tube diameter, which creates gaps between the tubes, on the loss of the fundamental core modes. The analogy to the slab waveguide sheds useful light on the mechanism of inhibited coupling in negative curvature fiber. However, this analogy is imperfect. In particular, a correct adjustment of the gap between the cladding tubes is important in minimizing the loss of the fundamental core mode. There is no analogous parameter in the slab waveguide. Simulation results that we present summarize work that is presented in [11,29,36,38,56,94,97,121,138].

In the waveguides that we will consider here, the true modes of the waveguide are the solutions of Maxwell's equations that are obtained by solving for the modes in the complete waveguide structure. All true modes are hybrid modes and are all mutually orthogonal (or, strictly speaking, biorthogonal once losses are taken into account). The true modes are neither pure core modes nor pure cladding modes, although the power in either the core or cladding region can be very low when coupling is inhibited between the core and the cladding. Alternatively, there are approximate modes that are the mode solutions of Maxwell's equations for the stand-alone core or cladding structures. The approximate modes reside almost entirely in the core or in the cladding. These approximate modes are not orthogonal and have a nonzero overlap that leads to mode coupling. Antiresonant reflection, discussed in Subsection 2.1, greatly reduces the overlap, but does not eliminate it. As long as the wavenumbers of the modes do not match, the effect of the overlap is weak, the approximate modes do not couple, and the true modes are well-approximated by the approximate core or cladding modes. However, when the wavenumbers match, an avoided crossing is created in which the true modes reside in both the core and the cladding. The loss of these hybrid modes

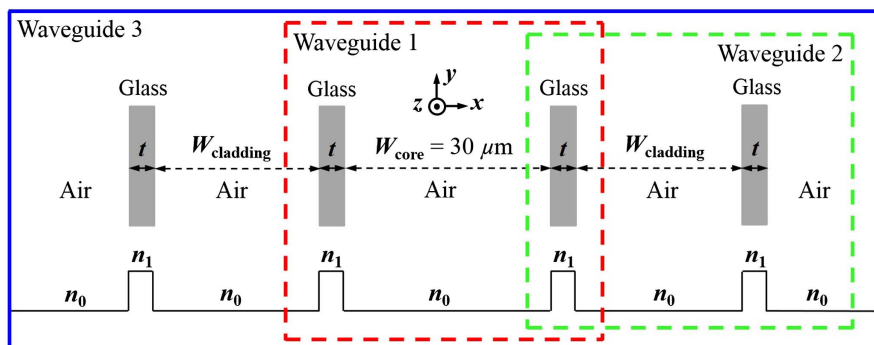
is typically far larger than the loss of modes that reside almost entirely in the core. If the overlap is weak, then the frequency range over which this resonant behavior occurs is restricted, but it will always be present when the wavenumbers match. To inhibit coupling, it is thus necessary to design waveguides that minimize the overlap between the core and cladding modes and in which the wavenumbers do not match over the frequency range of interest.

2.2a. Slab Waveguide

In this subsection, we describe inhibited coupling in a one-dimensional, three-layer slab waveguide with three air layers and four glass partitions. The three-layer slab waveguide is used here to study the mode coupling between the fundamental core mode that is between the two central glass partitions and the cladding mode that is between the two glass partitions on each side. Figure 15 shows the cross section and index profile of the waveguide. The thickness of the glass layers, t , is $0.72 \mu\text{m}$, which corresponds to the second antiresonant thickness that we described in the previous section. We focus here on leaky modes that exist primarily in the air slabs and have effective indices that are less than the air index of 1.0. There are glass modes with effective indices greater than 1.0, which we do not consider here. The true modes in this waveguide always exist in all three air slabs, as well as the glass. However, approximate modes that exist in the individual slabs can couple. The mode coupling in this simple slab waveguide is analogous to the mode coupling in negative curvature fibers between the fundamental core modes and the tube modes. The cladding modes in the slab waveguide are the modes in the stand-alone slab waveguide 2 that is shown in the green dashed box in Fig. 15. The approximate core modes in the stand-alone slab waveguide 2 will resemble the true cladding modes in the three-layer slab waveguide except near the avoided crossing.

The blue solid curve in Fig. 16(a) shows the effective index of the fundamental core mode as a function of the width of the air cladding, W_{cladding} , in the waveguide. The inner core width, W_{core} , is $30 \mu\text{m}$. The effective index of the true fundamental mode in waveguide 3 has three avoided crossings. The red and green dashed curves indicate the effective indices of the modes in the stand-alone, single-slab waveguide 1, and waveguide 2, respectively, and they overlap with the solid curve except at the avoided crossings. The loss of the true fundamental core mode in the three-layer slab waveguide 3 is shown in Fig. 16(b). The loss is high at $W_{\text{cladding}} = 30 \mu\text{m}$, $60 \mu\text{m}$, and $90 \mu\text{m}$, when the effective indices of the core mode and cladding modes match, as shown in Fig. 16(a).

Figure 15

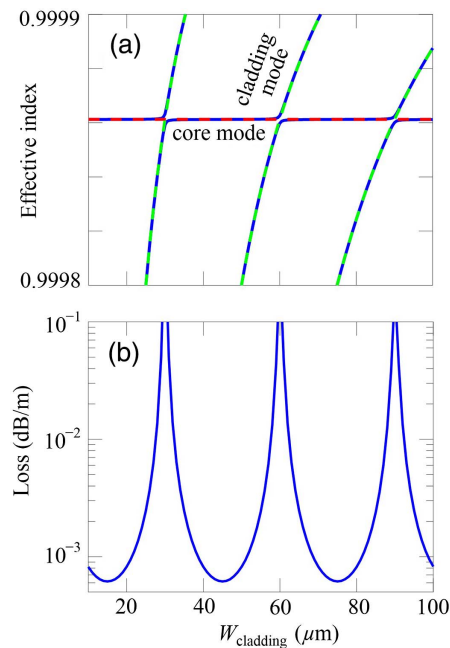


Cross section and index profile of a three-layer slab waveguide with four glass partitions. The red and green dashed boxes show the cross sections of the stand-alone slab waveguide 1 and waveguide 2, respectively.

The high loss at $W_{\text{cladding}} = 30 \mu\text{m}$, $60 \mu\text{m}$, and $90 \mu\text{m}$ can also be explained by the resonance condition in the low-index air cladding layer [31,33]. The fundamental core mode satisfies the resonance condition in the air core, $2k_T W_{\text{core}} = 2\pi$, where k_T is the transverse wave vector [139]. This resonance occurs because the phase change in one round trip of the air-core layer in the transverse direction is 2π [139]. When the low-index cladding layer satisfies the resonance condition $2k_T W_{\text{cladding}} = 2m\pi$, corresponding to $W_{\text{cladding}} = 30 \mu\text{m}$, $60 \mu\text{m}$, and $90 \mu\text{m}$, the leakage loss is high, as shown in Fig. 16(b). Thus, we find that resonance and antiresonance in the low-index layer induce strong coupling and inhibited coupling, respectively [31,33]. In negative curvature fibers, the thickness of the low-index layer cannot be exactly quantified; so, the analogy is not exact. However, it is qualitatively useful in understanding the role that antiresonance plays in inhibiting coupling between core modes and cladding modes.

Figure 17 shows a blow-up of the first avoided crossing near $W_{\text{cladding}} = 30 \mu\text{m}$ in Fig. 16(a). The two blue solid curves are effective indices of the two true modes in the three-layer slab waveguide in Fig. 15. The red and green dashed lines are the effective indices of the approximate modes in waveguide 1 and waveguide 2. When $W_{\text{cladding}} < 29 \mu\text{m}$, the indices of the two approximate modes do not match and the coupling is inhibited. The fields of the two true modes mainly reside in either waveguide 1 or waveguide 2. When $W_{\text{cladding}} = 30 \mu\text{m}$, the indices of the two approximate modes match and coupling occurs. The avoided crossing occurs and the two true modes become hybrid modes residing in both waveguide 1 and waveguide 2. When $W_{\text{cladding}} > 31 \mu\text{m}$, the indices of the two approximate modes do not match and the coupling is once again inhibited. The fields of the two true modes mainly reside in either waveguide 1 or waveguide 2. In the neighborhood of the

Figure 16

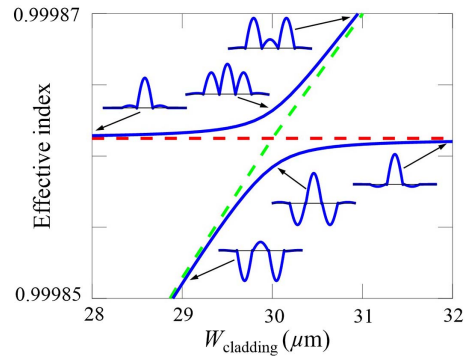


(a) Effective index of the true modes in the three-layer slab waveguide 3 (blue solid curve) and the stand-alone single-slab waveguide 1 (red dashed curve) and waveguide 2 (green dashed curve). (b) Leakage loss of the true fundamental core mode in the three-layer slab waveguide.

avoided crossing, the two true modes switch position between the waveguide 1 and waveguide 2 as W_{cladding} increases [121,138].

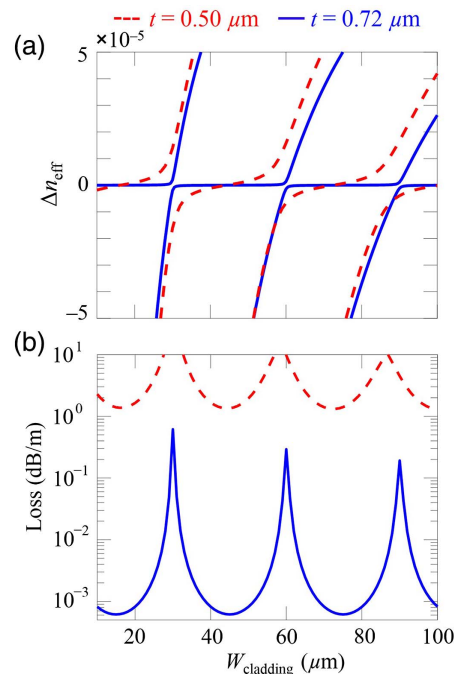
We studied antiresonant reflection using a one-layer slab waveguide in Subsection 2.1a. We now revisit antiresonance in the case of a three-layer slab waveguide. Figure 18 shows Δn_{eff} and the loss as W_{cladding} varies for glass thicknesses of 0.50 μm and 0.72 μm . These glass thicknesses correspond, respectively, to resonance

Figure 17



Effective indices of the air-slab modes in the three-layer slab near the avoided crossing at $W_{\text{cladding}} = 30 \mu\text{m}$. The insets show field distributions of the true modes in the three-layer slab.

Figure 18



(a) Effective index difference, Δn_{eff} , between the effective indices of the modes in waveguide 1 and waveguide 3, as illustrated in Fig. 15. The condition $\Delta n_{\text{eff}} = 0$ indicates that there is a mismatch between the wavenumbers of the approximate core and cladding modes in the three-layer slab waveguide. (b) Leakage loss of the true modes in the three-layer slab waveguide.

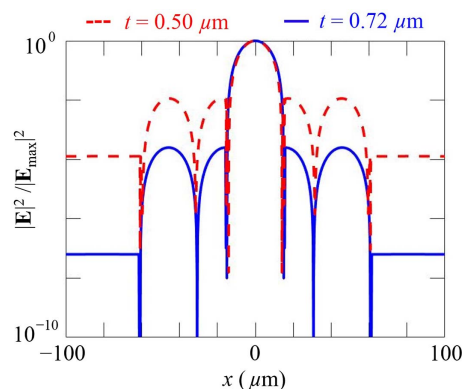
and to antiresonance, as shown in Fig. 4. We set $W_{\text{core}} = 30 \mu\text{m}$. The quantity Δn_{eff} is the difference between the effective indices in waveguide 1 and waveguide 3, as illustrated in Fig. 15. When $\Delta n_{\text{eff}} = 0$, the cladding layers do not affect the core layer, and the wavenumbers of the approximate core and cladding modes are mismatched. When the glass thickness t equals $0.50 \mu\text{m}$, the resonance condition is fulfilled, and coupling is strong for a wide range of values of W_{cladding} around which the effective indices of the approximate modes cross. For this range of values, we find $\Delta n_{\text{eff}} \neq 0$, as shown by the red dashed curves. When the glass thickness t equals $0.72 \mu\text{m}$, the antiresonance condition is fulfilled, and the range of values of W_{cladding} over which strong coupling occurs is greatly reduced, and the range of values for which $\Delta n_{\text{eff}} \neq 0$ is correspondingly reduced, as shown by the blue solid curves. Nonetheless, some wavenumber mismatch is needed. Figure 18(b) shows the leakage loss of the true fundamental modes in the three-layer slab waveguide, and we see that it always peaks when the effective indices of the approximate modes cross, but it is also consistently smaller when the antiresonance condition is met. Figure 19 shows the normalized electric field with $W_{\text{cladding}} = 45 \mu\text{m}$. We see that the field is higher in the cladding regions when the resonance condition is met, than it is when the antiresonance condition is met. That is consistent with the larger loss when the resonance condition is met. We conclude that while some wavenumber mismatch is needed between the approximate core and cladding modes, antiresonance plays a critical role in inhibiting coupling between these modes.

2.2b. Negative Curvature Fiber

In this subsection, we describe inhibited coupling in negative curvature fibers. We show the cross section of a negative curvature fiber with six cladding tubes in Fig. 20. The core diameter, D_{core} , is $30 \mu\text{m}$. The modes in a stand-alone annular core fiber, as shown in the red dotted box of Fig. 20, are approximate cladding modes in the negative curvature fiber.

Figure 21(a) shows the effective index of the true modes in the negative curvature fiber as a function of the gap, g , or the diameter of the cladding tubes, d_{tube} . The thickness of the cladding tubes, t , is $0.72 \mu\text{m}$, which corresponds to the antiresonance condition described in Subsection 2.1a. The blue solid curve and red solid curve show the effective indices of the true fundamental core mode and the true cladding tube mode, respectively. Note that core modes reside primarily in the central air core of the fiber, while tube modes reside primarily inside the cladding tubes. The effective indices of the true core mode and true cladding tube mode approach when the gap decreases and

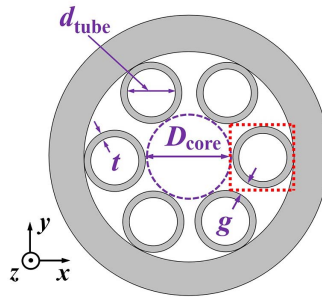
Figure 19



Normalized electric field intensity of the true modes in the three-slab waveguide with glass thicknesses of $0.50 \mu\text{m}$ and $0.72 \mu\text{m}$ and with $W_{\text{cladding}} = 45 \mu\text{m}$.

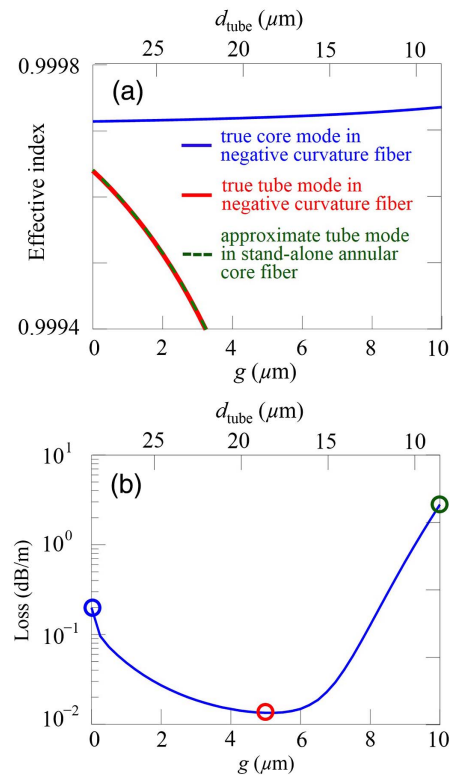
the tube diameter increases. The effective index of the approximate tube mode in the stand-alone annular core fiber is plotted using the green dashed curve, which matches the green dashed curve, which matches the true tube mode in the negative curvature fiber. There is no avoided crossing visible. The true modes are almost entirely in the core or in the cladding. It is not obvious how to define an approximate core mode in this case. However, we already showed in Subsection 2.1c that it corresponds to the mode of an annular core fiber in which the diameter is slightly larger than D_{core} . Figure 21(b) shows the loss of the true fundamental core mode in the negative curvature fiber. The loss is larger when there is no

Figure 20



Cross section of a negative curvature fiber with six cladding tubes. The red dotted box shows the cross section of the stand-alone annular core fiber.

Figure 21



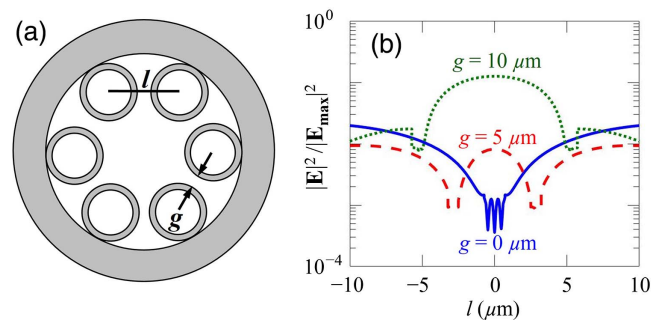
(a) Effective indices of the modes in the negative curvature fiber and the stand-alone annular core fiber. (b) Leakage loss of the fundamental core mode in the negative curvature fiber.

gap due to coupling to glass modes. The minimum loss occurs when the gap, g , is $5\ \mu\text{m}$. The loss is high with a larger tube diameter, which induces weak mode coupling between the fundamental core mode and the cladding tube modes [126]. It is analogous to the mode coupling in the three-layer slab waveguide that was described in Subsection 2.2a. However, there is no analogy to this gap in the slab waveguide that we considered in Subsection 2.2a.

The leakage loss increases as the gap increases from $5\ \mu\text{m}$ to $10\ \mu\text{m}$ due to leakage of the electric field through the air gap. Figure 22(b) shows the mode profile along the line connecting the center of two adjacent cladding tubes in the negative curvature fiber in Fig. 22(a) indicated by the black solid line. Similar plots have been presented in [56]. The mode intensity increases inside the gap when the gap increases from 0 to $10\ \mu\text{m}$. The increased leakage through the gap leads to an increased loss when the gap increases from $5\ \mu\text{m}$ to $10\ \mu\text{m}$ in Fig. 21(b).

There is no complete avoided crossing between the fundamental core mode and the tube mode in negative curvature fibers using six cladding tubes. The tube diameter, d_{tube} , the core diameter, D_{core} , the glass wall thickness of the cladding tubes, t , the minimum gap distance between the cladding tubes, g , and the number of tubes, p , are related by the expression $D_{\text{core}} = (d_{\text{tube}} + 2t + g)\sin(\pi/p) - (d_{\text{tube}} + 2t)$ [57,69,126,127,135]. For a fiber with six cladding tubes ($p = 6$), the core diameter has the relation, $D_{\text{core}} = d_{\text{tube}} + 2t + 2g$. The core diameter of the fiber is always larger than the tube diameter by twice the glass wall thickness and the gap between the cladding tubes, so that the effective index of the fundamental core mode is always larger than that of the tube mode. Hence, only part of an avoided crossing is seen near $g = 0\ \mu\text{m}$ in Fig. 21(a). We now examine negative curvature fibers with four cladding tubes. Figures 23(a) and 23(b) show a schematic illustration and mode effective index of a negative curvature fiber with four cladding tubes. We can see avoided crossings with gaps of $0\ \mu\text{m}$, $5\ \mu\text{m}$, or $11\ \mu\text{m}$. Note that the crossing [140,141] at a gap of $2\ \mu\text{m}$ occurs between the fundamental core mode and the cladding mode that is located in the interstices between the tubes and the outer glass ring, marked ε in Fig. 23(a). Figure 23(c) shows the leakage loss of the fundamental core mode. As expected, the loss of the fundamental core mode increases dramatically at the avoided crossing at a gap of $0\ \mu\text{m}$, $5\ \mu\text{m}$, or $11\ \mu\text{m}$. A small bump in the loss curve is observed at a gap of $2\ \mu\text{m}$ due to a match of the effective index and a mode overlap between the fundamental core mode and the interstice mode in the region marked ε in Fig. 23(a) [141]. A blow-up of this small bump is shown by the inset in Fig. 23(c). Comparison between

Figure 22

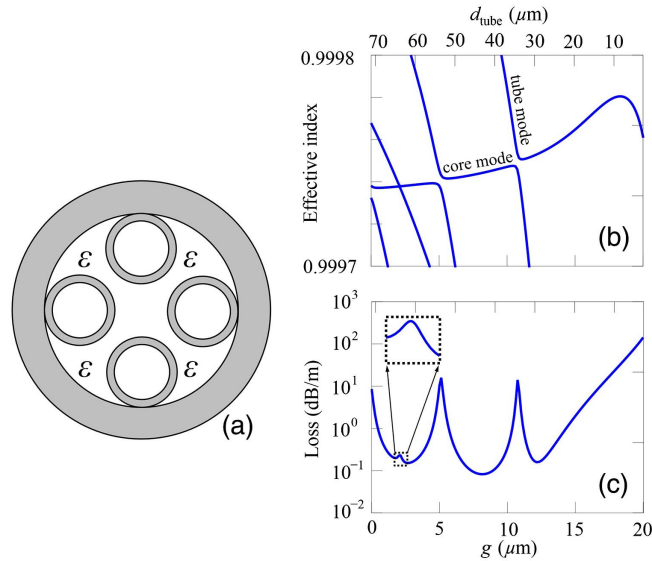


(a) Schematic illustration of a negative curvature fiber in which the black solid line connects the center of two adjacent cladding tubes. (b) The electric field intensity normalized to the electric field intensity in the center of the core at $g = 0\ \mu\text{m}$, $5\ \mu\text{m}$, and $10\ \mu\text{m}$, corresponding to the three circles in Fig. 21(b).

Figs. 21 and 23 shows that the coupling between the fundamental core mode and the tube mode is automatically avoided in negative curvature fibers using six cladding tubes with small air regions in the cladding outside the tubes. These small air regions in the cladding of the fibers that use six cladding tubes are helpful in inhibiting the coupling between the fundamental core mode and the cladding modes.

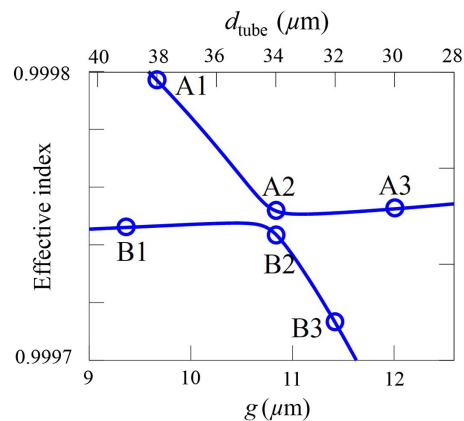
Figure 24 shows a magnification at the avoided crossing near a gap of 11 μm , as shown in Fig. 23(b). The two blue solid curves are effective indices of the two true modes in the negative curvature fibers. The corresponding mode field intensities at

Figure 23



(a) Cross section of a negative curvature fiber with four cladding tubes. (b) Effective index of different modes and (c) leakage loss of the fundamental core mode in the negative curvature fiber with four cladding tubes. Inset shows a blow-up of the loss around $g = 2 \mu\text{m}$.

Figure 24



Effective index of the fundamental core mode near the avoided crossing at $g = 11 \mu\text{m}$.

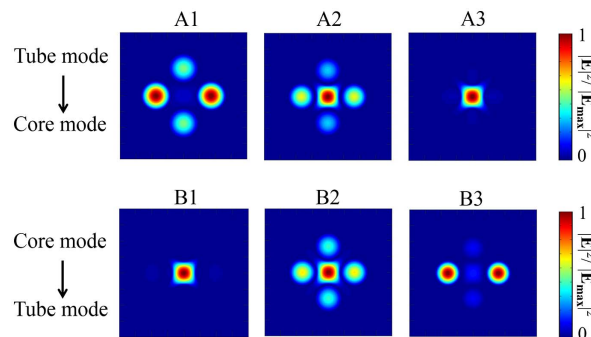
marked circles are shown in Fig. 25. We see avoided crossings that are analogous to the avoided crossings in the slab waveguide of Subsection 2.2a. While it is not obvious how to define an approximate core mode in this case, a study of the true modes shows that at gaps, g , that are far from the avoided crossings, the true modes reside almost entirely in the core or cladding, while at the avoided crossings, the true modes are hybrid modes that reside in both the core and the cladding. In the neighborhood of the avoided crossing, the two true modes switch position between the core and the cladding tubes as the gap increases or the tube diameter decreases [121,138].

While a negative curvature fiber with four cladding tubes is evidently easier to fabricate than a fiber with six or more cladding tubes, the existence of avoided crossings and the large loss that accompanies them make these fibers uninteresting in practice. This example illustrates once again that while antiresonance is necessary to inhibit coupling between core and cladding modes in negative curvature fibers, it is not sufficient.

2.3. Comparison of the Guiding Mechanisms in Photonic Bandgap and Negative Curvature Fibers

Hollow-core photonic bandgap fibers using a two-dimensional periodic cladding structure have attracted great interest due to their ability to transmit light power in the central air core [19,20]. A bandgap implies that certain frequencies are forbidden. If the light frequency is in the frequency range of the bandgap, the periodic cladding structure can confine the light in the central air core [13,14,18]. In addition, the effective index of the fundamental core mode will reside in the range of the bandgap [13,14,18,125,142]. Hence, the leakage loss can be reduced by simply adding more rings to the bandgap structures [143]. Currently, the lowest transmission loss in photonic bandgap fibers that has been demonstrated is 1.2 ~ 1.8 dB/km, which was achieved at around 1550 nm [18,21,43,144,145]. By taking advantage of inhibited coupling, the lowest losses that have currently been achieved in silica negative curvature fibers range from 7.7 dB/km to 50 dB/km at wavelengths between 0.75 μm to 3.39 μm [36,49–52,55–60]. It is difficult to arrange the antiresonant membranes to achieve coherent light reflection in the radial direction. Simply adding more tubes rings as is done in photonic bandgap fibers is not successful for negative curvature fibers due to the interconnecting struts or nodes [40,42]. A double antiresonant structure or a nested structure might provide a solution to this problem, as will be discussed in Subsection 3.5 [42,64,65,84,146].

Figure 25



Normalized electric field intensity near the avoided crossing at $g = 11 \mu\text{m}$, corresponding to the circles in Fig. 24.

In a bandgap fiber, light scattering in the bandgap region acts constructively to confine the light in the defect core. The nature of this guidance yields oscillatory light fields in the glass region [120,147]. Surface roughness on the interface between the glass and air created during the fiber cooling process dominates the loss in bandgap fibers [21,42,148]. In negative curvature fibers, the antiresonant glass membranes act as a mirror to reflect light back into the central core region. The outgoing and reflected light cancel out near the glass at the boundary of the core. Additionally, there is a wavenumber mismatch between the core and glass modes. As a consequence, coupling between the core mode and glass modes is inhibited, yielding a very low power ratio in the glass region of less than 0.01% [59,149]. Hence, surface scattering in negative curvature fibers can be possibly lower than in bandgap fibers. For the same reason, the power damage threshold is also expected to be higher in negative curvature fibers [150].

3. RECENT ADVANCES IN NEGATIVE CURVATURE FIBERS

We now discuss recent advances in the design of negative curvature fibers that improve the performance of the fibers, including negative curvature that increases confinement, gaps between tubes that increase confinement and bandwidth, additional tubes that decrease mode coupling, tube structures that suppress higher-order modes, nested tubes that increase guidance, and tube parameters that decrease bend loss. While the performance of these recent fiber designs is impressive, there are ways in principle to make the designs even better, which will increase the usefulness of these fibers.

3.1. Negative Curvature that Increases Confinement

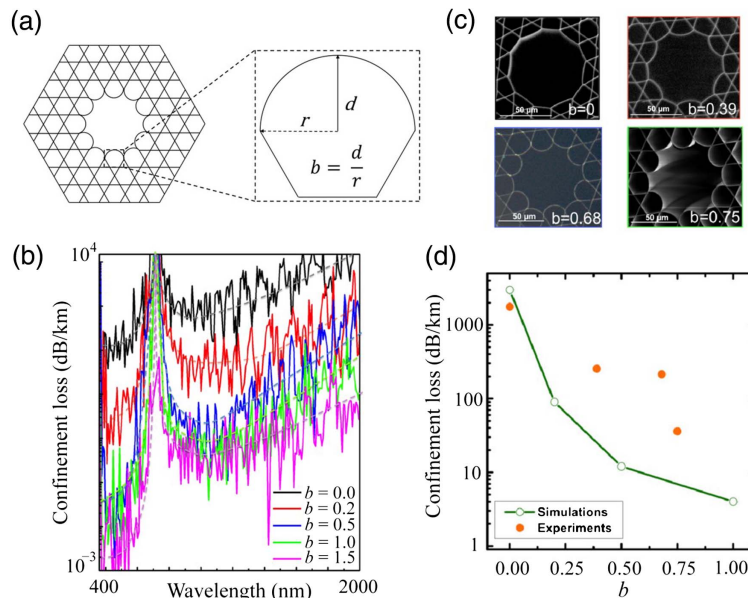
As explained in the Introduction, negative curvature fibers are one type of antiresonant fiber. The glass curvature surrounding the core has an impact on the leakage loss, bend loss, and coupling between the core mode and cladding modes [36,63]. This subsection will discuss the advantage of the negative curvature fibers of Debord *et al.* [36] relative to fibers with straight membranes in the inner core boundary. Numerical and experimental results are used to understand the influence of the arc curvature on the confinement loss in hypocycloid-shaped, hollow-core kagome photonic crystal fibers. Figure 26(a) shows a hypocycloid-like core in a silica kagome lattice cladding. The curvature of the hypocycloid-like core is quantified through the parameter, $b = d/r$, where d is the distance between the top of the arcs and the chord joining the nodes connecting the inward arc to the two neighboring arcs, and r equals half the chord length. The “classical” kagome fiber with a “quasi”-circular core corresponds to zero curvature, $b = 0$, while $b = 1.0$ corresponds to a circular core contour. Figure 26(b) shows the calculated loss spectra of the fundamental core mode with core arcs varying from $b = 0$ to $b = 1.5$ using the FEM [36]. The core inner radius R_{in} equals 30 μm . The simulation shows that the minimum leakage loss decreases as the curvature increases. This trend of decreasing loss with increasing curvature has been observed experimentally [36]. The effect of negative curvature increases the mode confinement and leads to a lower loss in negative curvature fibers [63,151–154]. Figure 26(c) shows SEM images of the fiber core with different curvature factors, b . Figure 26(d) shows qualitative agreement between the calculated confinement loss and the measured transmission loss at a wavelength of 1500 nm, when b increases from 0.0 to 1.0. The higher level of the measured loss relative to the numerical results is likely due to cladding imperfections, such as nonuniform strut thickness [36].

There are three major physical reasons behind the trend that is observed in Fig. 26 [36]. First, the spatial overlap of the optical power with the glass that surrounds the central core is reduced when the curvature increases. The relative power ratio in the

glass for the fundamental mode decreases by a factor of 10 when the curvature factor b increases from 0 to 0.5, and then decreases at a slightly lower rate when b increases from 0.5 to 2 [36]. The reduced overlap between the fundamental core mode and the glass indicates better confinement in the core region, and subsequently a decrease in the confinement loss. Second, the cladding mode with the effective index that is closest to that of the fundamental core mode has an intensity profile whose transverse phase oscillates rapidly with increasing curvature. The rapidly oscillating transverse phase inhibits the coupling between the fundamental core mode and the cladding modes. This inhibited coupling relies on a strong transverse mismatch between the core mode and cladding modes, and it leads to a reduction of the field overlap integrals and the leakage loss of the core mode [36,56]. Third, the increase of the curvature factor b induces higher loss for the higher-order modes while keeping lower loss for the fundamental mode. Hence, increase of the curvature factor leads to suppression of higher-order modes. The leakage loss of the fundamental core mode decreases as the curvature factor increases. The confinement loss of the higher-order modes increases as the curvature factor increases for $b > 0.5$, which is due to the coupling between the higher-order core mode and the tube modes, similar to what is shown in Subsection 3.4. Greater loss of higher-order modes is often desirable since it leads to a single mode after propagation.

The effect of negative curvature has also been studied in negative curvature fibers with elliptical cladding tubes [151–153]. A loss reduction of more than 1 order of magnitude has also been shown theoretically in fibers with elliptical cladding tubes compared to fibers using circular tubes [151–153].

Figure 26



(a) Structure of a hypocycloid-like core hollow-core PCF with definition of the parameters quantifying the curvature factor, b . (b) Confinement loss in kagome-lattice hollow-core PCF with arc curvatures $b = 0, 0.2, 0.5, 1.0$ and 1.5 . (c) SEM images of fabricated hypocycloid-core kagome-lattice hollow-core PCFs with different values of b . (d) Experimental and theoretical evolution of the transmission loss with respect to b at a wavelength of 1500 nm. Reprinted with permission from [36]. Copyright 2013 Optical Society of America.

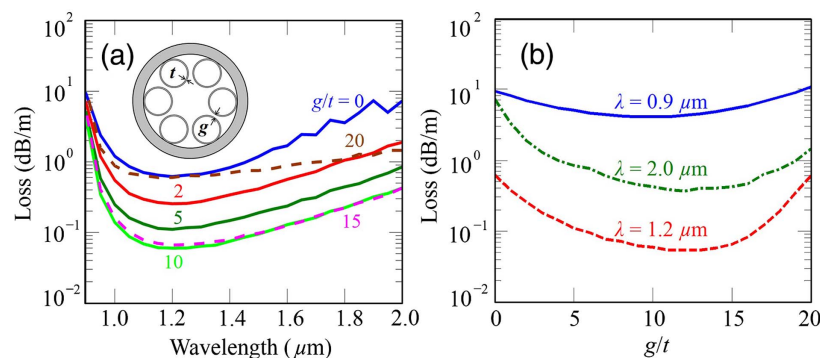
3.2. Gap Between Tubes that Increase Confinement and Bandwidth

Figures 1(e), 1(j), and 1(l) show fibers with no gap between the tubes, while Figs. 1(a)–1(d), 1(f)–1(i), 1(k), 1(n), and 1(o) show a gap or separation between the tubes. When the tubes are touching, localized nodes are created, and glass modes exist in these nodes. Separation between the cladding tubes eliminates additional resonances in the transmission bands [42,50].

Figure 27(a) shows the loss as a function of wavelength for a nodeless negative curvature fiber with six silica glass tubes in the cladding. The fiber parameters are core diameter, $D_{\text{core}} = 30 \mu\text{m}$; tube thickness, $t = 0.42 \mu\text{m}$; and refractive index of the glass, $n_1 = 1.45$. The minimum gap distance between the cladding tubes is denoted by g . The minimum loss, which is located in the middle of transmission band, increases as the gap-to-tube-thickness ratio, g/t , increases from 0 to 10 and then decreases when the gap-to-tube-thickness ratio, g/t , increases further. In order to better show this change, Fig. 27(b) shows the loss as a function of the gap-to-tube-thickness ratio, g/t , at wavelengths of $0.9 \mu\text{m}$, $1.2 \mu\text{m}$, and $2.0 \mu\text{m}$. At a wavelength of $0.9 \mu\text{m}$, which is not in the middle of the antiresonant transmission band, the gap does not significantly influence the loss. On the other hand, for wavelengths of $1.2 \mu\text{m}$ and $2.0 \mu\text{m}$, the loss can be decreased by up to one order of magnitude when g/t increases from 0 to 12. Therefore, the gap can be used to decrease the leakage loss in negative curvature fibers. A similar analysis applies to nested negative curvature fibers, where a decrease of 2 orders of magnitude in the loss can be obtained when an appropriate gap is used [42]. The reason for this decrease is that the mode in the nested negative curvature fiber is confined by two tubes in the same azimuthal direction, and the leakage loss is mainly determined by the gap.

Figure 28 shows the minimum loss and bandwidth as a function of the gap-to-tube-thickness ratio, g/t . The bandwidth is defined as the wavelength window in which the loss is less than twice the minimum loss. It can be seen that the minimum loss decreases and then increases as the g/t increases from 0 to 20. At a low value of g/t , the gap between the cladding tubes effectively eliminates the resonance in the touching nodes, but, when the gap increases, more light will leak out through the gap, and the confinement from the tubes becomes weaker. In order to have a loss less than 0.1 dB/m , the value of g/t should be between 5 and 15. At the same time, the bandwidth is between 0.5 to $0.6 \mu\text{m}$ when g/t increases from 0 to 15 and then increases sharply when g/t increases from 15 to 20. So, in order to obtain a wider bandwidth, the gap-to-tube-thickness ratio should be set between 15 and 20, depending on the

Figure 27



(a) Leakage loss as a function of wavelength for different gap-to-tube-thickness ratios, g/t . Inset is the geometry of the fiber. (b) Leakage loss as a function of the gap-to-tube-thickness ratio, g/t , for different wavelengths.

trade-off between loss and bandwidth in specific applications [42,126]. Similar results were also obtained in negative curvature fibers using chalcogenide glass [126]. The gap in negative curvature fibers inhibits coupling between the core and cladding modes until the gap becomes large enough for the light to leak through [56].

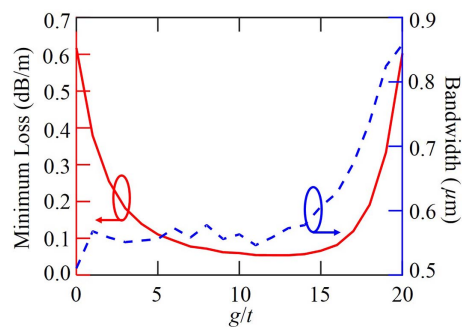
The operating wavelength range approximately equals 10% of the central wavelength in the bandgap fiber, which is limited by the bandgap [18,143,155]. In negative curvature fibers, the operating wavelength is located in between the nearby resonant wavelengths at $\lambda = 2t(n_1^2 - n_0^2)^{1/2}/m$, where m equals any positive integer and t is the tube wall thickness. Hence, in the case of small m , the operating wavelength range for antiresonant negative curvature fibers is wider than is the case for photonic bandgap fibers [36,42].

In the fiber drawing process, the surface tension straightens the tube walls [42]. Hence, it is difficult in practice to obtain touching circular tubes to produce a negative curvature core boundary. In a negative curvature fiber with nontouching tubes in the cladding, it is possible to keep the circular shape of the tubes even at a high drawing temperature [42]. Hence, fibers with a gap between tubes are easier to fabricate, since differential pressure and surface tension would naturally assist in maintaining the circular shapes of the tubes.

3.3. Additional Tubes that Decrease Mode Coupling

The previous subsection describes the leakage loss and bandwidth in a silica negative curvature fiber with six cladding tubes. This section describes the effect of the gap on the leakage loss in chalcogenide negative curvature fibers with different numbers of cladding tubes [126]. Figure 29(a) shows the leakage loss as a function of the gap for fibers with 6, 8, and 10 cladding tubes. The core diameter is 150 μm , and the wavelength is 5 μm . The refractive index of glass is 2.4 for As_2S_3 chalcogenide glass. The tube wall thickness is 1.8 μm to minimize the loss at a wavelength of 5 μm . For a fiber with six cladding tubes, the leakage loss decreases by a factor of 19 when a gap of 30 μm is used. For fibers with eight and 10 cladding tubes, the leakage loss decreases by only 66% and 49% when the gap increases from 0 to 10 μm , respectively. In order to explain this difference between fibers with 6, 8, and 10 cladding tubes, Fig. 29(b) shows the ratio of the power inside the tubes to the total power. For a fiber with six cladding tubes, the power ratio decreases by a factor of 3.8 when the gap increases from 0 to 10 μm . For fibers with eight and 10 cladding tubes, the power ratio only decreases by 22% and 21%, respectively, when the gap increases from 0 to 10 μm . This study shows that the gap has more impact on the power ratio for a fiber with six cladding tubes than it does for fibers with eight or 10 cladding tubes.

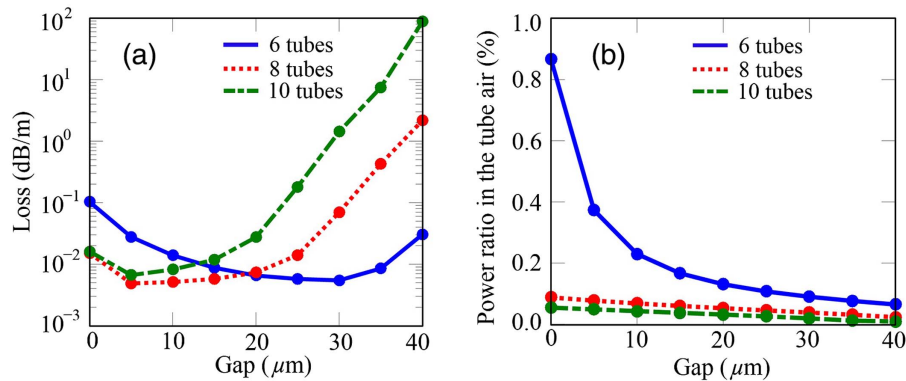
Figure 28



Minimum loss and bandwidth as a function of the gap-to-tube-thickness ratio, g/t .

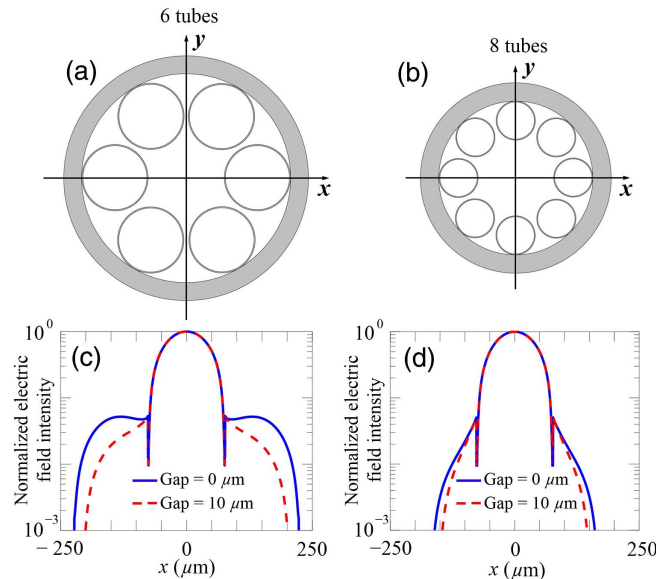
Figure 30 further shows the normalized electric field intensity at $g = 0 \mu\text{m}$ and $g = 10 \mu\text{m}$ in fibers with six and eight cladding tubes. Figure 30(a) shows the fiber geometry with six cladding tubes. Figure 30(c) shows the normalized electric field intensity in the fiber with six cladding tubes along the x -axis at $y = 0$. The mode is confined inside the core radius of $75 \mu\text{m}$ for both $g = 0 \mu\text{m}$ and $g = 10 \mu\text{m}$. The tube diameter is almost the same as the core diameter in a fiber with six cladding tubes. The field in the fiber with $g = 0 \mu\text{m}$ does not experience exponential decay inside the cladding tubes due to weak coupling between the central core mode and cladding tube modes,

Figure 29



(a) Leakage loss and (b) ratio of the power inside the tubes to total power as a function of the gap between tubes for fibers with 6, 8, and 10 cladding tubes. The tube wall thickness is $1.8 \mu\text{m}$ and the wavelength is $5 \mu\text{m}$. Reprinted with permission from [126]. Copyright 2015 IEEE.

Figure 30



Normalized electric field intensity at $g = 0 \mu\text{m}$ and $g = 10 \mu\text{m}$ in fibers with (a), (c) six and (b), (d) eight cladding tubes; (a) and (b) show the fiber geometries; (c) and (d) show the normalized electric field intensity along the x -axis at $y = 0$. The tube wall thickness is $1.8 \mu\text{m}$, and the wavelength is $5 \mu\text{m}$. Reprinted with permission from [126]. Copyright 2015 IEEE.

which is indicated by the blue solid curve. A gap of $10\ \mu\text{m}$ will effectively decrease the diameter of the cladding tubes and reduces the mode coupling between the central core mode and cladding tube modes. Hence, the field in a fiber with $g = 10\ \mu\text{m}$ decays exponentially inside the cladding tubes, which is indicated by the red dashed curve. For this reason, the ratio of the power inside the tubes to the total power decreases abruptly when the gap is introduced, as shown in Fig. 29(b). Figure 30(b) shows the fiber geometry with eight cladding tubes. In this case, the diameter of the tubes is much smaller than the diameter of the central air core. There is almost no coupling between the fundamental core mode and cladding tube modes, and the electric field intensities decay exponentially along the x -axis in the cladding tubes for both $g = 0\ \mu\text{m}$ and $g = 10\ \mu\text{m}$, as shown in Fig. 30(d). Hence, for a fiber with eight or 10 cladding tubes, there is no sharp decrease in the power ratio, as shown in Fig. 29(b). The power ratio decreases almost linearly when the gap increases from 0 to $40\ \mu\text{m}$. The optimal gap of $g = 5\ \mu\text{m}$ to $10\ \mu\text{m}$ for a fiber with eight or 10 cladding tubes is much smaller than the optimal gap of $30\ \mu\text{m}$ for a fiber with six cladding tubes, which is needed to remove the weak coupling between the fundamental core mode and cladding tube modes [126]. In Fig. 30, we show the light intensity with the electric field polarized in the x -direction. The other polarization yields the same conclusion.

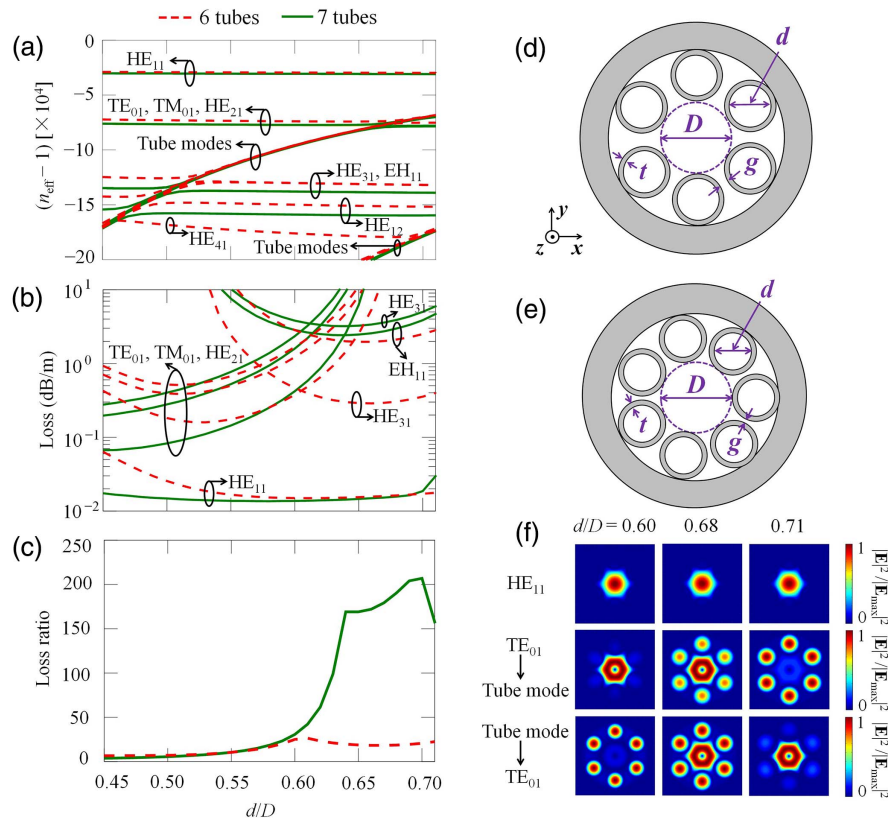
3.4. Tube Structures that Suppress Higher-Order Modes

The core diameters in negative curvature fibers are between $25\ \mu\text{m}$ and $380\ \mu\text{m}$ for fibers operating at visible and mid-IR wavelengths [48,50,54,61,79]. Large core sizes are often used to obtain a small leakage loss [42,156]. However, fibers with a large core diameter have higher-order core modes. It is desirable for many applications to suppress the higher-order modes, which decreases the coupling between the fundamental and higher-order core modes due to small perturbations like microbending [157,158]. The challenge is to suppress higher-order core modes while preserving low leakage loss for the fundamental core mode. This subsection describes higher-order mode suppression using resonant coupling between the higher-order core modes and the tube modes [57,69,79], while coupling of the fundamental mode to the tube modes remains inhibited. This approach is analogous to a rather complicated structure in a photonic bandgap fiber to create defect modes [157–160]; however, there is no need to create defects in negative curvature fibers, since the tubes that create the negative curvature can also provide resonant coupling. Avoided crossings lead to high loss for fiber modes [161,162]. It is possible to design negative curvature fibers so that an avoided crossing between the higher-order core modes and the fundamental tube modes leads to an increase in the loss of the higher-order core modes [36,42,57,65,69,79,151,163].

The fiber structures that have been studied consist of a central hollow core with a diameter of D surrounded by six or seven evenly spaced and nontouching cladding tubes with a wall thickness of t and an inner diameter of d , as shown in Figs. 31(d) and 31(e). The core diameter, D , is $30\ \mu\text{m}$, and the tube wall thickness, t , is $0.75\ \mu\text{m}$. The glass refractive index is set equal to 1.45, corresponding to silica at a wavelength of $1.0\ \mu\text{m}$, and the refractive index of hollow regions is set equal to 1.0. Figure 31(a) shows the effective indices of the fundamental core mode, the higher-order core modes, and the tube modes. The effective index of the HE_{11} core mode is high enough to avoid resonant coupling to the tube modes, and remains almost independent of d/D , whereas the TE_{01} , TM_{01} , and HE_{21} core modes couple strongly with the tube mode at $d/D = 0.68$, leading to avoided crossings. The losses for the fundamental core modes, the higher-order core modes, and the tube modes are plotted in Fig. 31(b). For fibers with six cladding tubes, an HE_{31} core mode becomes the lowest-loss higher-order core mode when $d/D > 0.61$. Michieletto *et al.* [57] showed that, for fibers with

seven cladding tubes, the HE_{31} core modes have a higher loss due to the mismatch of the symmetry between the HE_{31} modes [136] and the fiber geometry with seven cladding tubes. In this case, the EH_{11} mode becomes the lowest-loss higher-order core mode when $d/D > 0.64$. Figure 31(c) shows the loss ratio of the lowest-loss higher-order core modes to the HE_{11} core mode. For fibers with six cladding tubes, the highest loss ratio of 28 occurs at $d/D = 0.61$ between the fundamental HE_{11} mode and the higher-order HE_{31} mode. For fibers with seven cladding tubes, the highest loss ratio of 200 occurs at $d/D = 0.70$ between the fundamental HE_{11} mode and the higher-order EH_{11} mode. The decrease of the loss ratio at $d/D = 0.71$ is due to the increase of loss of the HE_{11} core mode with a very small gap between cladding tubes. In order to study the coupling mechanism between the higher-order core modes and tube mode, Fig. 31(f) shows the normalized mode field intensity of the HE_{11} core mode, the TE_{01} core mode, and the tube mode coupled with the TE_{01} core mode at $d/D = 0.60, 0.68,$ and 0.71 in fibers with six cladding tubes. When $d/D = 0.60$, both the TE_{01} core mode and the corresponding tube mode are well-confined to the core and the tubes, respectively. When $d/D = 0.68$, in the center of the parameter range in which the avoided crossing occurs, both the original TE_{01} core mode and

Figure 31



(a) Effective indices of the fundamental core mode, the higher-order core modes, and the tube modes. (b) Losses of the fundamental HE_{11} core modes and the higher-order core modes. (c) Loss ratio of the higher-order core modes with the lowest loss to the fundamental HE_{11} core mode. Schematic illustration of the cross section of a negative curvature fiber with (d) six and (e) seven cladding tubes. (f) Normalized electric field intensity at $d/D = 0.6, 0.68,$ and 0.71 . Figures 31(a) to 31(c) are reproduced using parameters from [57]. Reprinted with permission from [57]. Copyright 2016 Optical Society of America

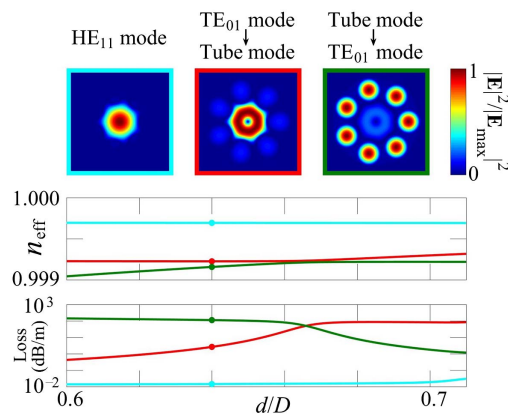
corresponding tube mode reside partly in the core and partly in the cladding tubes. Both have effectively become hybrid modes. When d/D further increases to 0.71, the original TE_{01} core mode shifts into the tubes and the original tube mode shifts into the core. By contrast, the HE_{11} core mode remains almost unaffected by the avoided crossing. The leakage loss of the fundamental HE_{11} core mode is still 0.02 dB/m. In Fig. 32 (Visualization 1), we show a movie of the mode variation in a fiber with seven cladding tubes as d/D increases from 0.6 to 0.7 for the HE_{11} core mode, the TE_{01} core mode, and the tube mode coupled with the TE_{01} core mode.

Similar higher-order mode suppression can also be found using increased curvature in hypocycloid-shaped kagome hollow-core photonic crystal fibers [36], using nested tubes [42,65,164,165], using chalcogenide glass fibers with different tube thicknesses [69], using one ring of tubes with different tube diameters [79], using twisted fibers [166], using a semi-circular cladding structure [167], and using elliptical cladding tubes [151,152]. The higher-order core modes can also be analyzed using the spatially and spectrally resolved imaging in negative curvature fibers [60,81,168–172].

3.5. Nested Tubes that Increase Guidance

In Figs. 1(a)–1(m), there is only one negative curvature antiresonant structure used in the radial direction. One may ask whether it is possible to add another set of tubes outside of the existing tubes to decrease the leakage loss, just as in the case of solid-core photonic crystal fiber in which the leakage loss is reduced by adding more air-hole rings. Unfortunately, just simply adding another ring of tubes in the hexagonal structure creates many unwanted localized nodes and does not lower the leakage loss [40,42]. One solution to this problem is to add another tube inside the existing tube lattice at the same azimuthal angle. This double antiresonant fiber maintains the nodeless tube lattice structure, but it includes more nested tubes with the same thickness as the outer ones, attached to the cladding at the same azimuthal position, as shown in the bottom part of Fig. 33(a) [42]. In this fiber, two antiresonant reflections are created due to the double negative curvatures at the inner and outer glass tubes. These double antiresonant negative curvature fibers were proposed by Belardi and Knight [64] and by Poletti [42]. The main difference between these two studies is that the structure in [42] has a separation between the major tubes. The benefit of using nested elements becomes evident when the field and leakage loss of the modes that are guided in the

Figure 32

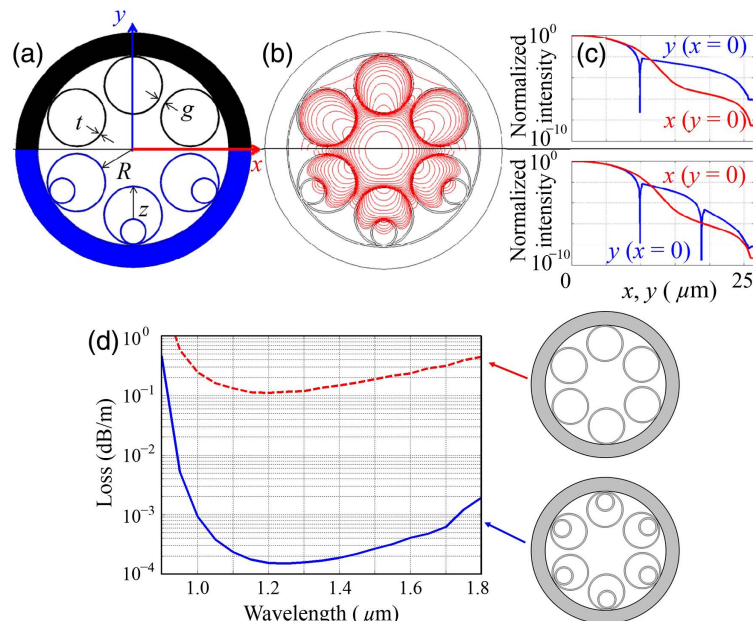


Movie (Visualization 1) of the mode variation in a fiber with seven cladding tubes as d/D increases from 0.6 to 0.7 for the HE_{11} core mode, the TE_{01} core mode, and the tube mode coupled with the TE_{01} core mode.

two structures are compared. Figure 33(b) shows that the additional antiresonant membrane is effective in improving the field confinement of the mode to the core, along both radial directions where the resonant tubes are present (y -axis) and in between the tubes (x -axis) [42]. Figure 33(c) compares the normalized fundamental mode intensities in the two fibers with single (upper figure) and double (lower figure) tubes, calculated along two orthogonal x - and y -directions [42]. The intensity is normalized to the intensity in the center. The mode intensity decays in both the x - and y -directions. If we look at the blue curve for the y -direction at $y = 25 \mu\text{m}$, the intensity in the fiber with nested elements is 2 orders of magnitude lower than the intensity in the fiber without nested elements. Figure 33(d) shows a comparison of the leakage loss of the fibers with and without nested elements. The leakage loss of the fiber with nested elements has a minimum value of only 0.2 dB/km, which is 3 orders of magnitude lower than the loss in the fiber without nested elements. All fibers have the same core radius $R = 15 \mu\text{m}$, uniform strut thickness $t = 0.42 \mu\text{m}$, gap $g = 5t$, and separation between inner and outer tubes $z = 0.9R$. The material of the fiber is silica with a refractive index of 1.45. Hence, the addition of the nested elements helps achieve lower leakage loss. A similar decrease in the loss of annular core fibers can be achieved by using two or three concentric rings [28]. By adding a second ring with the same wall thickness as that of the single ring of an annular core fiber, coupling to the cladding modes is inhibited, and the leakage loss can be decreased by 2 orders of magnitude [28].

Nested negative curvature fibers have been fabricated using silica glass [61,84]. Higher-order mode suppression and bend loss have also been studied [42,64,65,164,165]. There has been additional research on nested negative curvature fibers, including multiple nested fibers [42,64,65], semi-circular nested fibers

Figure 33



Comparison between single antiresonant negative curvature fiber and double antiresonant negative curvature fiber: (a) structure, (b) 3 dB contour plots, and (c) intensity. (d) Confinement loss comparison between single antiresonant and double antiresonant fibers. (d) This figure is regenerated using the parameters from [42]. Reprinted with permission from [42]. Copyright 2014 Optical Society of America.

[146,154], elliptical nested fibers [164], and adjacent nested fibers [65]. It has been found that nested tubes do not increase mode confinement when the diameters of the nested tubes are less than 4–5 times the wavelength because the nested tubes no longer act as an antiresonant layer [127]. Negative curvature fibers with cladding tubes using composite glass layers have also been proposed and fabricated [173].

3.6. Tube Parameters that Decrease Bend Loss

Bend loss is another important issue for fibers, as bending is hard to avoid in practical application. This issue is of particular importance for hollow-core fibers with large mode diameters. It is preferable for a fiber to be insensitive to bends when it is used for light delivery. Conversely, however, bend sensitivity can be useful for sensing [135]. The bend loss for a photonic bandgap fiber mainly comes from the fiber structure's distortion. In negative curvature fibers, besides the structure's distortion, coupling between the core mode and tube modes can lead to an increase in the loss of the core modes [37,42,67,68,82,174]. Structures that include nested cladding tubes or smaller cladding tubes have been proposed to decrease the bend loss [42,68]. Bending-induced higher-order mode suppression has been obtained using the resonant coupling between the higher-order core modes and the tube modes in negative curvature fibers [57,175]. This subsection shows a comparison of the bend losses in two fundamental modes whose polarization directions are parallel or perpendicular to the bend direction [135]. Fiber bends break the symmetry of the fiber geometry, and the two fundamental core modes become nondegenerate modes in bent negative curvature fibers. The bend is assumed to be along the x -axis. Due to the reflection symmetry with respect to the $y = 0$ plane, a fiber geometry in which $y > 0$ is used in simulations [136]. A conformal transformation is used in calculations to replace the bent fiber with a straight fiber that has an equivalent index distribution: $n'(x, y) = n(x, y) \cdot \exp(x/R)$, where R is the bend radius [68,176]. The core diameter is 150 μm , the tube wall thickness is 1.8 μm , the minimum gap between the cladding tubes is 10 μm , and the wavelength is 5 μm . The real part and imaginary part of the complex index of refraction of As_2S_3 chalcogenide glass are 2.4 and 3.4×10^{-8} , respectively [177]. Figures 34(a) and 34(b) show the effective indices and bend losses for core modes at different bend radii. There are two avoided crossings and two high-loss peaks in the effective index curves and bend loss curves at bend radii of 5.7 cm and 9.4 cm for both the parallel-polarized and perpendicular-polarized modes with respect to the bend direction.

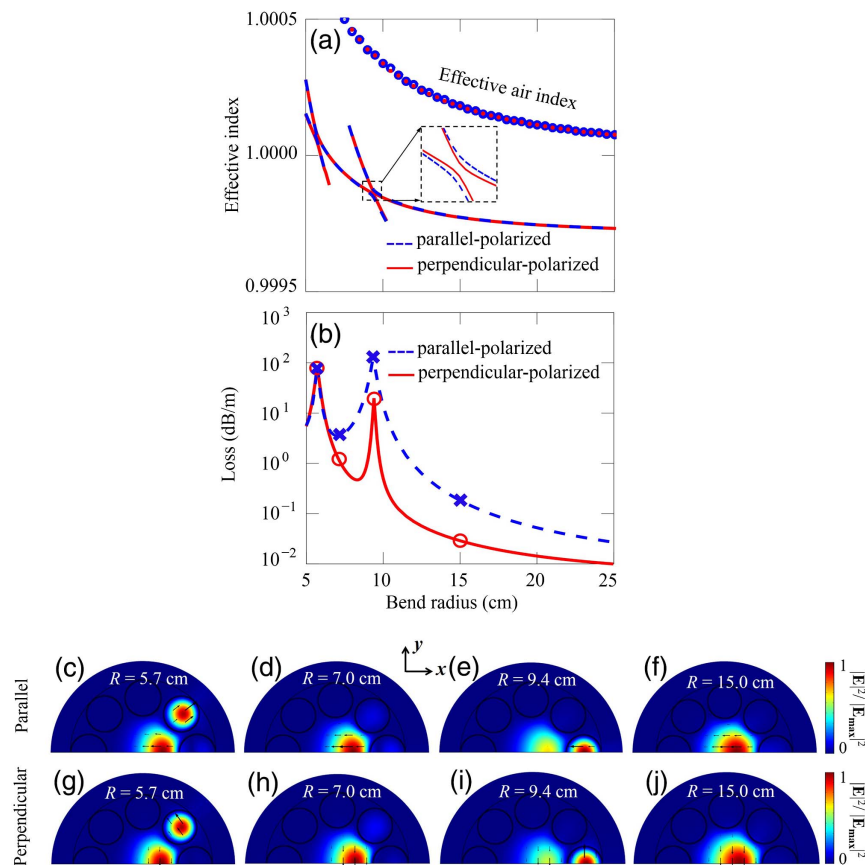
The first bend loss peak at 5.7 cm is almost the same for the parallel-polarized and perpendicular-polarized modes. By contrast, the second bend loss peak at 9.4 cm is higher for the parallel-polarized mode than it is for the perpendicular-polarized mode. Examining the mode structure allows us to explain this difference. Figures 34(c)–34(f) and 34(g)–34(j) show both the parallel-polarized and perpendicular-polarized modes at the bend radii of 5.7 cm, 7.0 cm, 9.4 cm, and 15.0 cm, corresponding to the four crosses and four circles, respectively, in Fig. 34(b). At a bend radius of 9.4 cm, coupling occurs between the core mode and the tube mode, which is located along the bend direction, as indicated by Figs. 34(e) and 34(i). The bend loss of the parallel-polarized mode is higher than the bend loss of the perpendicular-polarized mode, as shown in Fig. 34(b). The alignment of the core mode and the coupled tube mode is the same as the polarization direction for the parallel-polarized mode. Therefore, the coupling is stronger for the parallel-polarized mode and leads to a loss that is up to a factor of 6 higher than the loss of the perpendicular-polarized mode when the bend radius is 15 cm and is up to a factor of 28 higher when the bend radius is 10 cm. Since both parallel-polarized and perpendicular-polarized core modes are coupled to the same tube modes, avoided crossings and loss peaks occur at the same bend radius of

9.4 cm, as indicated by Figs. 34(a) and 34(b). At a smaller bend radius of 5.7 cm, the index in the tube along the bend direction is higher than the core index. Index matching occurs between the core mode and the tube mode at 45 deg with respect to the bend direction or x -axis, as indicated by Figs. 34(c) and 34(g) [82,135,178]. Since both the core modes in the two polarizations are coupled to the tube mode at 45 deg with respect to their polarization directions, those two nondegenerate modes have almost the same loss at the same bend radius of 5.7 cm, as shown in Fig. 34(b).

The modes at the bend radii of 7.0 cm and 15.0 cm do not couple, as shown in Figs. 34(d), 34(h), 34(f), and 34(j). The fundamental mode is well-confined in the core in these cases. Conversely, coupling between the core and tube mode is visible when the bend radius equals 9.4 cm in Figs. 34(e) and 34(i). Hence, the bend loss peaks in Fig. 34(b) are induced by the mode coupling between the core and tube modes in the negative curvature fiber [68,69].

Photonic bandgap fibers were reported to have a bend loss of 0.25 dB/turn for a bend radius of 2.5 cm with a core diameter of 50 μm and a wavelength greater than 3.35 μm

Figure 34



(a) Effective indices and (b) bend losses for both parallel-polarized and perpendicular-polarized modes in a negative curvature fiber with a tube wall thickness of 1.8 μm . The effective air index is defined as the index after conformal transformation at the peak of the core mode intensity. (c)–(j) The parallel-polarized and perpendicular-polarized modes at bend radii of 5.7 cm, 7.0 cm, 9.4 cm, and 15.0 cm. The contour plots represent the normalized electric field intensity, and the arrows represent the amplitude and direction of the transverse electric field. Reprinted with permission from [135]. Copyright 2016 Optical Society of America.

[179]. Since the cladding air holes are much smaller than the central air core in the bandgap fiber, the mode matching between the core mode and cladding mode does not induce much leakage loss [180]. The bend loss for the bandgap fibers mainly comes from the structure distortion, which affects the periodicity of the bandgap. In negative curvature fibers, a small distortion in the fiber structure or tube thickness still yields comparable confinement, as shown in Fig. 13. The bend loss mainly comes from the mode coupling between the core mode and the tube mode. Hence, making a smaller tube size [68] or adding more nested elements [42] in the negative curvature fibers will effectively decrease the effective index of the tube mode, which will decrease the coupling-induced bend loss. By introducing a gap between the cladding tubes and using smaller tubes compared to the core size, the bend loss can be reduced to 0.15 dB/turn and 0.25 dB/turn for a bend radius of 8 cm and 2.5 cm, respectively, with a core diameter of 109 μm at a wavelength of 3.35 μm [68]. Bend losses of 0.8 dB/turn and 0.02 dB/turn at a bend radius of 5 cm and a wavelength of 1500 nm were found for hypocycloid-shaped kagome hollow-core fibers with one and four cladding rings [37]. A bend loss of 0.05 dB/turn was found at a bend radius of 3 cm and a wavelength of 1064 nm for negative curvature fibers with seven cladding tubes [57]. A bend loss of 0.03 dB/turn was found at a bend radius of 5 cm and a wavelength of 1550 nm for negative curvature fibers with six cladding tubes [178,181].

4. APPLICATIONS

In this section, we will present applications of negative curvature fibers, including mid-IR fiber lasers, micromachining, and surgical procedures.

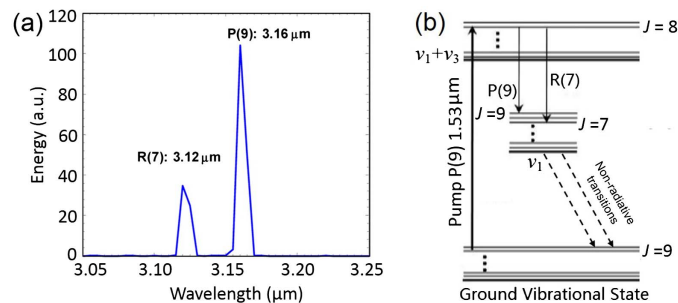
4.1. Mid-IR Fiber Lasers

Optically pumped molecular lasers are effective wavelength converters for generating coherent radiation at mid-IR wavelengths [83,91,182]. The invention of hollow-core fibers and their ability to host gases for long interaction lengths and micrometer-scale mode areas have enabled new gas-filled hollow-core fiber lasers. This subsection describes the work by Wang *et al.* [83] on mid-IR emission that has been achieved using acetylene-filled hollow-core negative curvature fibers. In this work, the fiber had a core diameter of 109 μm , a tube diameter of 27.9 μm , a silica wall thickness of 2.4 μm , and a fiber length of 10.5 m. The pump diode laser had a wavelength of 1530.37 nm, a repetition rate of 10 kHz, and a pulse duration of 20 ns. The loss at the pump wavelength of 1.53 μm was 0.11 dB/m. The loss was 0.1 dB/m near the output laser wavelengths of 3.1–3.2 μm . The coupling efficiency was 80%. The gain fiber was filled with acetylene using two gas cells. The output optical spectrum is shown in Fig. 35(a). The vibrational modes are sketched in Fig. 35(b). There are different rotational states, marked by J , in each of the vibrational states. Acetylene molecules are first excited by the pump pulses from the $J = 9$ rotational state of the ground vibrational state to the $J = 8$ rotational state of the $\nu_1 + \nu_3$ vibrational state [83]. This pumping creates an immediate population inversion between the $J = 8$ rotational state in the $\nu_1 + \nu_3$ vibrational state and the empty ν_1 vibrational state. The molecules can leave the $\nu_1 + \nu_3$ vibrational state through a radiative transition to a ν_1 vibrational state. The two lasing lines at wavelengths of 3.12 μm and 3.16 μm in Fig. 35(a) correspond to the transmissions R(7) and P(9) in Fig. 35(b), respectively. Here, $R(J)$ and $P(J)$ are used to refer to transitions $J + 1 \rightarrow J$ and $J - 1 \rightarrow J$, respectively, where J is the rotational quantum number of the lower vibrational state [183]. There is no direct path for the population in the terminal excited state to transfer to or from the ground vibrational state during the pump duration [184,185]. Figure 36 shows that the laser pulse energy increases nearly linearly with the absorbed pump

pulse energy beyond the threshold. The absorption coefficient is 95% with a long interaction length in the hollow-core fiber. If one plots the laser pulse energy as a function of incident pump energy, the slope of the curves will not decrease significantly. The minimum pump pulse energy that is required to observe an output was below 50 nJ and the maximum output average laser power was 7.6 mW corresponding to a pulse energy of 0.76 μJ . With a larger pressure, the calculated mean free path of acetylene molecules is much smaller than the core size of the fiber, so that intermolecular collisions are dominant.

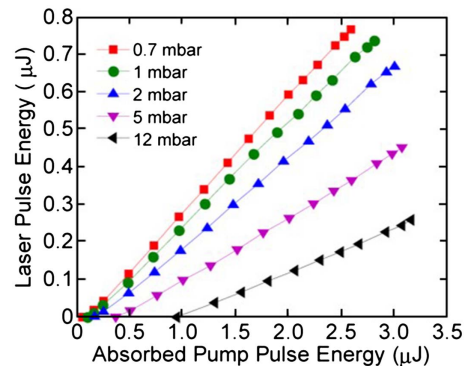
By properly designing the fiber's transmission bands, and carefully selecting active gases and pump lasers, efficient, compact, high-power mid-IR fiber gas lasers can potentially be obtained at a number of wavelengths. Negative curvature fibers with a low transmission loss, a wide bandwidth, a large core size, and a high damage threshold can play an important role in hollow-core gas fiber lasers [185,186]. In addition, the pulse propagation in the hollow-core fiber has a very low nonlinearity, which can be used to increase the cavity length of the fiber laser loop. In this case, the fiber laser repetition rate can be decreased with no degradation of the pulse peak power or pulse shape [187].

Figure 35



(a) Measured output optical spectrum of $^{12}\text{C}_2\text{H}_2$ acetylene at a pressure of 0.7 mbar, a fiber length of 10.5 m, and an incident pump energy of 4.2 μJ . (b) Simple energy level diagram of $^{12}\text{C}_2\text{H}_2$ acetylene, showing the pump and laser transitions. Reprinted with permission from [83]. Copyright 2014 Optical Society of America.

Figure 36



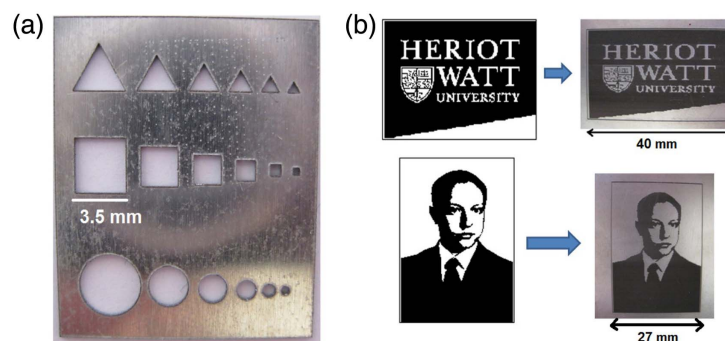
Output laser emission pulse energy as a function of the absorbed pump pulse energy at different acetylene pressures. Reprinted with permission from [83]. Copyright 2014 Optical Society of America.

4.2. Micromachining

High-power lasers are widely used in micromachining because of their accuracy and flexibility. Unfortunately, nonlinearity limits high-power delivery in solid-core optical fibers. Hollow-core fibers confine the light inside a hollow air core surrounded by a photonic crystal cladding, which can provide low-loss and high-power transmission [21]. Negative curvature fibers, as one kind of hollow-core fiber, can be used for high-power delivery by taking advantage of low nonlinearity, a high damage threshold, and low material absorption because most of the light power propagates in the air core. Jaworski *et al.* [53] showed that high-average-power picosecond and nanosecond pulse delivery using negative curvature fibers can be used for micromachining. The fiber used in this experiment was a silica negative curvature hollow-core fiber fabricated by the common stack and draw technique, described in [49]. The fiber had a length of 10.5 m and an attenuation of 0.16 dB/m at 1064 nm. A diode-pumped Spectra Physics *Q*-switched Nd:YVO₄ laser was used to generate pulses at a wavelength of 1064 nm, with an energy of 0.8 mJ, a duration of 60 ns, and a repetition rate of 15 kHz. The spot diameter of the focused laser was calculated to be 30 μm. Figure 37 shows the precise cutting of an aluminum sheet and marking on titanium, using laser pulses transmitted by a negative curvature fiber. The edge is neat and clear on the aluminum sheet with a thickness of 0.3 mm. The cutting speeds were 1 mm/s for the aluminum cutting and 100 mm/s for the titanium marking. High-quality shapes were generated, and no thermal damage to the surrounding material was observed.

Experiments were also carried out to demonstrate high-quality machining of 0.15 mm thick fused silica using a TRUMPF TruMicro picosecond laser, as shown in Fig. 38(a). The wavelength was 1030 nm, the duration was 6 ps, the pulse energy was 52 μJ, and the repetition rate of the laser pulses was 400 kHz. The fiber had a length of 1 m and an attenuation of 0.23 dB/m at 1030 nm. Figure 38(a) shows the micromilled pattern using a picosecond laser pulse that is transmitted by a negative curvature fiber with no cracks on the glass sample. The spot diameter of the focused laser at the workpiece was calculated to be 36 μm and the marking speed was 100 mm/s, which makes it possible to fabricate features with the dimensions less than 1 mm × 1 mm with a depth of 30 μm. It is hard to achieve crack-free machining of glass with picosecond pulses that are delivered at wavelengths near 1 μm using solid-core large-mode-area fibers or conventional hollow-core fibers due to the low damage threshold and non-linear effects in the short pulse regime. Later, 10 m long kagome fibers were also used for laser micromachining in glass sheet, as shown in Fig. 38(b) [188].

Figure 37



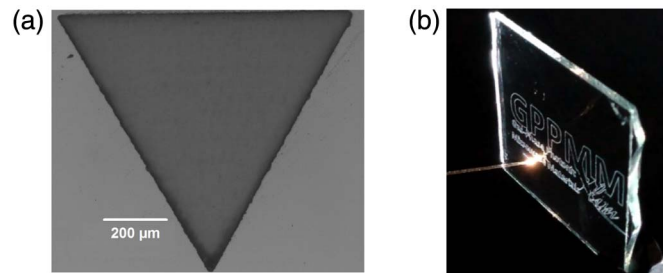
(a) Cutting of a 0.3 mm thick aluminum sheet, and (b) marking on a titanium using laser pulses transmitted by negative curvature fibers. Reprinted with permission from [53]. Copyright 2013 Optical Society of America.

Precision machining experiments at wavelengths of 532 nm and 515 nm were also carried out in negative curvature fibers [189]. The energy threshold damage was measured to be 5 mJ level in hypocycloid-shaped kagome fibers [190,191]. The energy handling capability of these fibers is higher than that of standard hollow-core bandgap fibers [92] and conventional silica fibers. Hence, negative curvature fibers provide a strong candidate for a solution to high power handling requirements.

4.3. Surgical Procedures

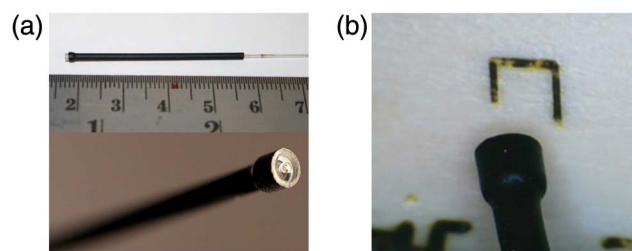
Biological tissue with water absorbs mid-IR radiation very well. Mid-IR lasers can offer a safe, effective, and precise surgical cutting tool for minimally invasive surgical procedures [192,193]. The benefit includes small penetration depth, high precision, no additional pressure, and a minimal heat-affected zone to reduce collateral damage and cell death in surrounding tissue [194,195]. A flexible transmission tool from the laser to the patient is required for successful surgery, and optical fibers are good candidates, because of their small size, weight, and flexibility. This subsection describes the work by Urich *et al.* [52,196] on high-energy delivery through a negative curvature fiber, which can be used for soft and hard tissue ablation under both dry and aqueous conditions. The geometry of this negative curvature fiber is the same as the fiber in Fig. 1(m) with a core diameter of 94 μm [49]. The attenuation of this fiber is 34 dB/km at a wavelength of 3.05 μm . An Impex High Tech ERB 15 laser was used to generate optical pulses at a wavelength of 2.937 μm , a full width at half-maximum

Figure 38



(a) Example of a micromilled pattern in a fused silica using negative curvature fiber to deliver optical pulses. Reprinted with permission from [53]. Copyright 2013 Optical Society of America. (b) A frame from the video showing glass sheet engraving from a laser beam directly delivered from a hypocycloid-shaped kagome fiber. Reprinted with permission from [188]. Copyright 2014 Optical Society of America.

Figure 39



(a) A fiber mounted with the end tip using a heat shrinking tube. (b) Ablation of ovine bone in air. Reprinted with permission from [52]. Copyright 2013 Optical Society of America.

of 225 μs , and a repetition rate of 15 Hz. The laser light has a focused spot size diameter of 67 μm . The maximum coupling efficiency achieved was around 35% due to a mismatch between the laser mode and fiber mode profiles. A total fiber length of 6.5 m was used, where 5.5 m of the fiber was coiled with a diameter of 0.5 m. The fiber attenuation was measured to be 0.183 dB/m at a wavelength of 2.94 μm . In order to avoid fiber contamination, the fiber end was encapsulated with a sapphire end tip, which was mounted onto the fiber using a heat-shrinking tube, as shown in Fig. 39(a). The output power was 30 mJ at 2.94 μm at the surface of the end tip with a divergence half-angle of 36 mrad and an energy density of larger than 500 J/cm² at the contact point. This energy density far exceeds the ablation thresholds necessary for biological tissue. At the same time, this energy density is well within the operating capability of the device. Using this fiber system with an end tip, soft tissue in muscle and hard tissue in bone can be ablated in both air and water. The ablation of ovine bone in air is shown in Fig. 39(b). The width of the cut is around 300 μm , and the depth of the cut is 220 μm . This system for high-power applications at 2.94 μm demonstrates a promising surgical device for minimally invasive surgical procedures.

Laser poration can remove the barrier skin layer, and thereby provides a route for the diffusion of applied drugs [197]. Femtosecond pulsed laser ablation was demonstrated to enhance drug delivery across the skin [198]. A negative curvature fiber was used to deliver femtosecond pulsed visible light. The optical nonlinearity and dispersive effects in conventional step-index fibers are too high for this application [198]. Light guided in the negative curvature fibers is confined to an air core with low nonlinearity and dispersion, which allows the delivery of high-peak-power femtosecond pulses [199].

5. FUTURE PROSPECTS

Due to their ability to transmit light with low loss over a broad bandwidth and with low fiber nonlinearity, negative curvature fibers have many potential applications [200,201]. We expect extensive research to continue in future years in the areas of data communications, power delivery, nonlinear optics, chemical sensing, bend sensing, as well as mid-IR, ultraviolet (UV), and THz transmission.

In data communications, conventional step-index fibers provide large transmission bandwidth and low transmission loss. However, light propagates about 30% slower in a silica glass fiber than in the vacuum. Air guidance in a hollow-core fiber can reduce fiber latency significantly [156,202]. Additionally, the wavelength-division multiplexing bandwidth in a step-index fiber is limited by material absorption. High transmission capacity of 1.48 Tbit/s and 24 Tbit/s has been demonstrated using hollow-core photonic bandgap fibers [202,203]. In photonic bandgap fibers, the effective index of the core mode must be inside the frequency range of the bandgap so that the bandwidth is smaller than the bandwidth of negative curvature fibers [42,59]. A negative curvature fiber can significantly increase the data bandwidth of an optical fiber interconnect if the fiber can achieve suitably low loss [51,126]. A combination of low loss and wide bandwidth in negative curvature fibers may play a key role in high-capacity data transmission [59].

In negative curvature fibers, most of the power is located in air, which does not contribute to the nonlinearity. Energy damage thresholds of 3.2 mJ and 5 mJ were measured using lasers at a wavelength of 1064 nm and a pulse duration of 9 ns [53,190]. Transmission of 30 mJ pulses was also reported using lasers at a wavelength of 1064 nm and a pulse duration of 30 ns [204]. Such a high damage threshold will enable new applications requiring high-power delivery, such as cutting, welding, and engraving [53,205]. Dispersion was also studied in negative curvature fibers

for high-energy femtosecond pulse delivery [99,206,207]. Low dispersion was obtained in hypocycloid-shaped kagome fibers with different silica thicknesses [99]. A low dispersion slope was also found in negative curvature fibers because of strong field localization in the air core in a femtosecond pulse transmission experiment [206]. Negative curvature fibers with low dispersion and nonlinearity can also deliver the light for multiphoton microscopy, where optical pulses with an ultrashort duration and a broad wavelength range are required to efficiently excite a diverse range of fluorophores [208].

The ability of negative curvature fibers to deliver high power makes it possible to do nonlinear optics experiments in fiber cores that are filled with gases, vapors, and plasmas, which is not possible using conventional fibers based on total internal reflection [24,209–214]. Gas-filled negative curvature fibers are particularly suited for ultrafast nonlinear fiber optics because of their ability to guide high-intensity light due to their high glass damage threshold, as explained in Subsection 4.1 [83]. Supercontinuum generation in the UV and mid-IR regions has been studied using gas-filled negative curvature fibers [215,216]. In addition, experiments can be carried out using different gases in negative curvature fibers, leading to different gas-filled fiber laser sources. Mid-IR gas-filled kagome fiber lasers have been made using C_2H_2 , HCN, and I_2 [91,93,184,217]. Stimulated Raman scattering has been demonstrated in a 1 m long hollow-core photonic crystal fiber filled with hydrogen gas [24]. Experiments using negative curvature fibers filled with ethane and hydrogen gases have demonstrated efficient 1.5 μm , 1.9 μm , and 4.4 μm emission from stimulated Raman scattering [102,218–223]. Three-octave spectral comb, spanning wavelengths from 325 nm to 2300 nm, has been generated and guided, using a hydrogen-filled hollow-core photonic crystal fiber [29]. A hypocycloid-shaped kagome fiber filled with hydrogen was also used to generate Raman comb, which spans from 370 nm to 1150 nm covering the whole visible wavelength range [224]. Soliton–plasma interactions have also been studied in a gas-filled kagome hollow-core PCF and negative curvature fibers [213,225]. High-power transmission in negative curvature fibers can also be used for pulse compression [206,226–229].

Liquid-filled and gas-filled hollow-core PCFs can provide strong light confinement, an enhanced reaction rate, and a long interaction length for chemical sensing experiments [26,230–233]. Low-loss liquid-filled photonic bandgap fibers have an intrinsic limitation due to a narrow transmission window, which makes Raman or fluorescence spectroscopy experiments difficult [80]. The micrometer-scale hole size can make the liquid filling process time-consuming, especially for large clusters or viscous liquids [80]. In addition, enlarging the core size in photonic bandgap fibers for the same operational wavelength requires removing additional elements from the core and adds complexity to the fabrication procedure [42,234]. In negative curvature fibers, core scaling can happen with no additional fabrication complexity [42]. The larger tubes in negative curvature fibers make the liquid filling procedure easier [80,230]. Gas sensing of acetylene, hydrogen cyanide, methane, and ammonia have been demonstrated in hollow-core bandgap fibers [232,235–238]. By appropriately choosing the photonic crystal fiber parameters, high-sensitivity gas detection should be possible. Since the absorption region of most gases is at mid-IR wavelengths, the ability of negative curvature fibers to transmit light in the mid-IR makes them attractive for gas-sensing applications.

The bend loss of the two polarization modes in negative curvature fibers can differ significantly, as shown in Subsection 3.6 [135]. This differential bend loss could be used to make bending sensors [239,240], in which the bend in the transverse direction is quantified by monitoring the losses in the two polarizations. Hence, negative curvature fibers can be used in highly sensitive optical bending sensor systems.

Negative curvature fibers are promising for applications in different wavelength ranges, including the UV, visible, IR, and THz ranges. Infrared fibers have become increasingly prominent in a variety of scientific disciplines and technological applications, such as chemical sensing, environmental monitoring, homeland security, and medical diagnostics [74,241,242]. In standard silica fibers, light does not propagate beyond 2 μm . Thus, nonsilica glasses must be used for infrared applications [74]. In negative curvature fibers, only a small amount of power overlaps with the glass region. Hence, the material loss in the glass has only a limited impact on the propagation loss, which is the reason that negative curvature fibers made of silica can still have low loss in the mid-IR region at wavelengths of 3.4 μm and 4.0 μm [50,51]. Theoretical research shows that, at wavelengths shorter than 4.5 μm , silica negative curvature fibers have a leakage loss that is around or below 0.1 dB/m and are preferable to chalcogenide fibers [127]. At wavelengths longer than 4.5 μm , it is preferable to use As_2S_3 chalcogenide or As_2Se_3 chalcogenide negative curvature fibers since their leakage loss is one or more orders of magnitude lower than the loss of silica negative curvature fibers [127]. The development of hollow-core chalcogenide fibers has been hampered by fabrication difficulties [78]. Negative curvature fibers have a simpler structure than photonic bandgap fibers, which makes it easier in principle to fabricate them [54,76]. We expect to see more research on negative curvature fibers using non-silica glasses.

The UV regime has turned out to be of essential importance for a vast number of applications, such as Raman microscopy [243–245], photochemistry [231], and lithography [246]. The small overlap with the glass region will make it possible to use negative curvature fibers in UV applications [104,113].

THz transmission has been studied in tube lattice fibers [82,109,110,247–249], kagome fibers [250], Bragg fibers [251], thin-wall pipe waveguides [117,118,252], photonic bandgap fibers [253], and antiresonant fibers [254,255]. Guiding the electromagnetic radiation inside a hollow-core fiber is helpful in reducing the propagation loss in this case. A THz spectroscopy and imaging system has been demonstrated using a polymer hollow-core negative curvature fiber [256]. We expect that negative curvature fibers will be used in more THz [257] and spectroscopy [258] applications.

Polarization-maintaining fiber is a specialty fiber with a strong built-in birefringence. Such fiber is used in applications where preserving polarization state in transmission is essential. Research shows that the birefringence is small in negative curvature fibers whose cladding is composed by an elliptical arrangement of circular dielectric tubes [259]. In particular, the birefringence is always low when the wavelength is close to the center of the transmission windows [259]. Higher birefringence and differential loss can be achieved in negative curvature fibers with more additional nested tubes using different thicknesses in the core boundary [146,260,261].

Most of the theoretical study on hollow-core photonic crystal fibers uses ideal structures, which provides a good reference for the experiment. In experiments, structural distortions have significant impact on fiber properties such as bandwidth and leakage loss. The properties of air-core photonic bandgap fibers depend sensitively on the structural parameters [262–264]. The main reason is that the confinement in photonic bandgap fibers requires a periodic cladding. Any distortion of the structure in the cladding region will affect the periodic bandgap structure. In negative curvature fibers, theoretical results show that tube diameter and glass thickness may play a noticeable role on the fiber loss [59,61,265]. Variations in these perturbations along the longitudinal axis of the fiber could significantly increase the loss over a wide bandwidth [265]. More effort in the theoretical study of cladding imperfections will lead to a better understanding of the requirements for fiber drawing.

6. SUMMARY

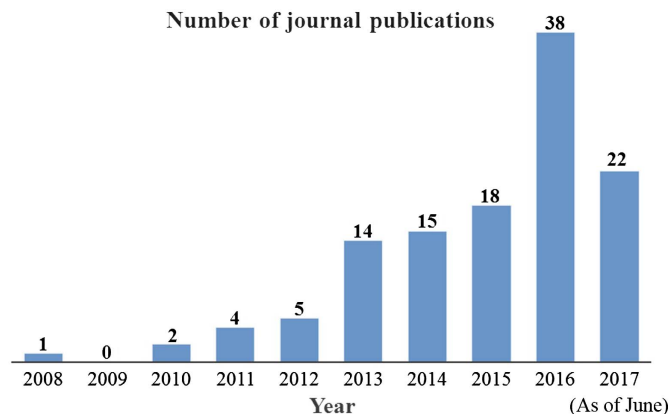
Negative curvature fibers have drawn much attention in recent years. Figure 40 shows the number of journal articles in the references of this review article related to hollow-core fibers that use a negative curvature inner core boundary. Steady growth over the years indicates the growing interest in this field. Due to the fabrication complexity, only a handful of groups are able to fabricate photonic bandgap fibers. On the contrary, due to their relative simplicity, more groups can fabricate negative curvature fibers consisting of one ring of tubes [266].

In this review paper, we show simulation results for the mode properties and the transmission loss in slab waveguides, annular core fibers, and negative curvature fibers. The geometries with glass thicknesses corresponding to antiresonance have low leakage loss. The leakage loss in negative curvature fibers is 3 orders of magnitude lower than the leakage loss in annular core fibers due to the negative curvature in the core boundary. The effect of negative curvature leads to a lower loss in negative curvature fibers [63,151–154] by inhibiting coupling between the fundamental core mode and the cladding modes [36,56]. There are two elements that are needed to obtain low loss. First, the overlap between the approximate modes must be small. Antiresonance helps make that happen. Second, one must use a fiber structure, in which the wavenumber of the approximate fundamental core mode is not matched to any of wavenumbers of the approximate cladding modes. No matter how small the overlap is, the approximate modes will always couple strongly when the wavenumbers match. The combination of antiresonance in the glass at the core boundary and a wavenumber mismatch with the cladding modes has led to remarkably low loss in negative curvature fibers.

We have described recent advances in negative curvature fibers, including the use of negative curvature that increases confinement, gaps between tubes that increase confinement and bandwidth, additional tubes that decrease mode coupling, tube structures that suppress higher-order modes, nested tubes that increase guidance, and tube parameters that decrease bend loss.

The advances in the negative curvature fibers enable a large range of applications, including mid-IR fiber lasers, micromachining, and surgery. Negative curvature fibers will be the best choice for a wide range of different applications because of their combined advantages of low loss, broad bandwidth, and a low power ratio in the glass.

Figure 40



Number of journal publications in the references of this review article related to hollow-core fibers that use a negative curvature inner core boundary.

FUNDING

Baylor Young Investigator Development Award (YIDA); U.S. Naval Research Laboratory (NRL); Max-Planck Institute for the Physics of Light.

ACKNOWLEDGMENT

J. H. thanks G. S. Agrawal for pointing out Ref. [139]. J. H. thanks R. A. Kuis and F. Chenard for useful discussions. Work by C. W. and J. H. on negative curvature fibers has been supported by the Baylor YIDA. Work by R. J. W. and C. R. M. on negative curvature fibers has been supported by the NRL. Part of the work of C. R. M. was carried out while he was a guest at the Max-Planck Institute for the Physics of Light in Erlangen, Germany with support from the Alexander von Humboldt Foundation. C. R. M. thanks A. Abdolvand and P. St.J. Russell for useful discussions on negative curvature fibers.

REFERENCES

1. P. V. Kaiser and H. W. Astle, "Low-loss single-material fibers made from pure fused silica," *Bell Syst. Tech. J.* **53**, 1021–1039 (1974).
2. J. D. Joannopoulos, S. G. Johnson, J. N. Winn, and R. D. Meade, *Photonic Crystals: Molding the Flow of Light* (Princeton University, 2011).
3. E. Yablonovitch, "Inhibited spontaneous emission in solid-state physics and electronics," *Phys. Rev. Lett.* **58**, 2059–2062 (1987).
4. S. John, "Strong localization of photons in certain disordered dielectric superlattices," *Phys. Rev. Lett.* **58**, 2486–2489 (1987).
5. J. C. Knight, T. A. Birks, P. St.J. Russell, and D. M. Atkin, "Pure silica single-mode fiber with hexagonal photonic crystal cladding," in *Conference on Optical Fiber Communications* (Optical Society of America, 1996), postdeadline paper PD3.
6. J. C. Knight, T. A. Birks, P. St.J. Russell, and D. M. Atkin, "All-silica single-mode optical fiber with photonic crystal cladding," *Opt. Lett.* **21**, 1547–1549 (1996).
7. T. A. Birks, J. C. Knight, and P. St.J. Russell, "Endlessly single-mode photonic crystal fiber," *Opt. Lett.* **22**, 961–963 (1997).
8. N. W. Aschcroft and N. D. Mermin, *Solid State Physics* (Saunders College, 1976).
9. S. L. Altmann, *Band Theory of Solids: An Introduction from the Point of View of Symmetry* (Clarendon, 1994).
10. F. Couny, F. Benabid, P. J. Roberts, M. T. Burnett, and S. A. Maier, "Identification of Bloch-modes in hollow-core photonic crystal fiber cladding," *Opt. Express* **15**, 325–338 (2007).
11. F. Benabid and P. J. Roberts, "Guidance mechanisms in hollow-core photonic crystal fiber," *Proc. SPIE* **6901**, 69010U (2008).
12. F. Zolla, G. Renversez, A. Nicolet, B. Kuhlmeiy, S. Guenneau, D. Felbacq, A. Argyros, and S. Leon-Saval, *Foundations of Photonic Crystal Fibres*, 2nd ed. (Imperial College, 2012).
13. P. St.J. Russell, "Photonic crystal fibers," *Science* **299**, 358–362 (2003).
14. P. St.J. Russell, "Photonic-crystal fibers," *J. Lightwave Technol.* **24**, 4729–4749 (2006).
15. T. A. Birks, D. Mogilevtsev, J. C. Knight, and P. St.J. Russell, "Dispersion compensation using single-material fibers," *IEEE Photon. Technol. Lett.* **11**, 674–676 (1999).
16. P. Yeh and A. Yariv, "Bragg reflection waveguides," *Opt. Commun.* **19**, 427–430 (1976).

17. P. Yeh, A. Yariv, and E. Marom, "Theory of Bragg fiber," *J. Opt. Soc. Am.* **68**, 1196–1201 (1978).
18. F. Poletti, M. N. Petrovich, and D. J. Richardson, "Hollow-core photonic bandgap fibers: technology and applications," *Nanophotonics* **2**, 315–340 (2013).
19. J. C. Knight, J. Broeng, T. A. Birks, and P. St.J. Russell, "Photonic band gap guidance in optical fibers," *Science* **282**, 1476–1478 (1998).
20. R. F. Cregan, B. J. Mangan, J. C. Knight, T. A. Birks, P. St.J. Russell, P. J. Roberts, and D. C. Allan, "Single-mode photonic band gap guidance of light in air," *Science* **285**, 1537–1539 (1999).
21. P. J. Roberts, F. Couny, H. Sabert, B. J. Mangan, D. P. Williams, L. Farr, M. W. Mason, A. Tomlinson, T. A. Birks, J. C. Knight, and P. St.J. Russell, "Ultimate low loss of hollow-core photonic crystal fibres," *Opt. Express* **13**, 236–244 (2005).
22. C. M. Smith, N. Venkataraman, M. T. Gallagher, D. Müller, J. A. West, N. F. Borrelli, D. C. Allan, and K. W. Koch, "Low-loss hollow-core silica/air photonic bandgap fibre," *Nature* **424**, 657–659 (2003).
23. J. D. Shephard, J. D. C. Jones, D. P. Hand, G. Bouwmans, J. C. Knight, P. St.J. Russell, and B. J. Mangan, "High energy nanosecond laser pulses delivered single-mode through hollow-core PBG fibers," *Opt. Express* **12**, 717–723 (2004).
24. F. Benabid, J. C. Knight, G. Antonopoulos, and P. St.J. Russell, "Stimulated Raman scattering in hydrogen-filled hollow-core photonic crystal fiber," *Science* **298**, 399–402 (2002).
25. P. St.J. Russell, P. Hölzer, W. Chang, A. Abdolvand, and J. C. Travers, "Hollow-core photonic crystal fibres for gas-based nonlinear optics," *Nat. Photonics* **8**, 278–286 (2014).
26. F. Benabid, F. Couny, J. C. Knight, T. A. Birks, and P. St.J. Russell, "Compact, stable and efficient all-fibre gas cells using hollow-core photonic crystal fibres," *Nature* **434**, 488–491 (2005).
27. F. Couny, F. Benabid, and P. S. Light, "Large-pitch kagome-structured hollow-core photonic crystal fiber," *Opt. Lett.* **31**, 3574–3576 (2006).
28. G. J. Pearce, G. S. Wiederhecker, C. G. Poulton, S. Burger, and P. St.J. Russell, "Models for guidance in kagome-structured hollow-core photonic crystal fibres," *Opt. Express* **15**, 12680–12685 (2007).
29. F. Couny, F. Benabid, P. J. Roberts, P. S. Light, and M. G. Raymer, "Generation and photonic guidance of multi-octave optical-frequency combs," *Science* **318**, 1118–1121 (2007).
30. A. Argyros and J. Pla, "Hollow-core polymer fibres with a kagome lattice: potential for transmission in the infrared," *Opt. Express* **15**, 7713–7719 (2007).
31. M. A. Duguay, Y. Kokubun, T. L. Koch, and L. Pfeiffer, "Antiresonant reflecting optical waveguides in SiO₂/Si multilayer structures," *Appl. Phys. Lett.* **49**, 13–15 (1986).
32. Y. Kokubun, T. Baba, T. Sakaki, and K. Iga, "Low-loss antiresonant reflecting optical waveguide on Si substrate in visible-wavelength region," *Electron. Lett.* **22**, 892–893 (1986).
33. N. M. Litchinitser, A. K. Abeeluck, C. Headley, and B. J. Eggleton, "Antiresonant reflecting photonic crystal optical waveguides," *Opt. Lett.* **27**, 1592–1594 (2002).
34. N. M. Litchinitser, S. C. Dunn, B. Usner, B. J. Eggleton, T. P. White, R. C. McPhedran, and C. M. de Sterke, "Resonances in microstructured optical waveguides," *Opt. Express* **11**, 1243–1251 (2003).
35. T. P. White, R. C. McPhedran, C. M. Sterke, N. M. Litchinitser, and B. J. Eggleton, "Resonance and scattering in microstructured optical fibers," *Opt. Lett.* **27**, 1977–1979 (2002).

36. B. Debord, M. Alharbi, T. Bradley, C. Fourcade-Dutin, Y. Y. Wang, L. Vincetti, F. Gérôme, and F. Benabid, "Hypocycloid-shaped hollow-core photonic crystal fiber Part I: arc curvature effect on confinement loss," *Opt. Express* **21**, 28597–28608 (2013).
37. M. Alharbi, T. Bradley, B. Debord, C. Fourcade-Dutin, D. Ghosh, L. Vincetti, F. Gérôme, and F. Benabid, "Hypocycloid-shaped hollow-core photonic crystal fiber Part II: cladding effect on confinement and bend loss," *Opt. Express* **21**, 28609–28616 (2013).
38. A. Argyros, S. G. Leon-Saval, J. Pla, and A. Docherty, "Antiresonant reflection and inhibited coupling in hollow-core square lattice optical fibers," *Opt. Express* **16**, 5642–5648 (2008).
39. F. Couny, P. J. Roberts, T. A. Birks, and F. Benabid, "Square-lattice large-pitch hollow-core photonic crystal fiber," *Opt. Express* **16**, 20626–20636 (2008).
40. S. Février, B. Beaudou, and P. Viale, "Understanding origin of loss in large pitch hollow-core photonic crystal fibers and their design simplification," *Opt. Express* **18**, 5142–5150 (2010).
41. F. Gérôme, R. Jamier, J.-L. Auguste, G. Humbert, and J.-M. Blondy, "Simplified hollow-core photonic crystal fiber," *Opt. Lett.* **35**, 1157–1159 (2010).
42. F. Poletti, "Nested antiresonant nodeless hollow core fiber," *Opt. Express* **22**, 23807–23828 (2014).
43. P. J. Roberts, D. P. Williams, B. J. Mangan, H. Sabert, F. Couny, W. J. Wadsworth, T. A. Birks, J. C. Knight, and P. St.J. Russell, "Realizing low loss air core photonic crystal fibers by exploiting an antiresonant core surround," *Opt. Express* **13**, 8277–8285 (2005).
44. G. Pearce, J. Pottage, D. Bird, P. Roberts, J. Knight, and P. St.J. Russell, "Hollow-core PCF for guidance in the mid to far infra-red," *Opt. Express* **13**, 6937–6946 (2005).
45. R. Amezcua-Correa, N. G. Broderick, M. N. Petrovich, F. Poletti, and D. J. Richardson, "Design of 7 and 19 cells core air-guiding photonic crystal fibers for low-loss, wide bandwidth and dispersion controlled operation," *Opt. Express* **15**, 17577–17586 (2007).
46. Y. Wang, F. Couny, P. J. Roberts, and F. Benabid, "Low loss broadband transmission in optimized core-shaped Kagome hollow-core PCF," in *Conference on Lasers and Electro-Optics (CLEO)*, OSA Technical Digest (CD) (Optical Society of America, 2010), paper CPDB4.
47. Y. Y. Wang, N. V. Wheeler, F. Couny, P. J. Roberts, and F. Benabid, "Low loss broadband transmission in hypocycloid-core Kagome hollow-core photonic crystal fiber," *Opt. Lett.* **36**, 669–671 (2011).
48. A. D. Pryamikov, A. S. Biriukov, A. F. Kosolapov, V. G. Plotnichenko, S. L. Semjonov, and E. M. Dianov, "Demonstration of a waveguide regime for a silica hollow-core microstructured optical fiber with a negative curvature of the core boundary in the spectral region $>3.5 \mu\text{m}$," *Opt. Express* **19**, 1441–1448 (2011).
49. F. Yu, W. J. Wadsworth, and J. C. Knight, "Low loss silica hollow core fibers for 3–4 μm spectral region," *Opt. Express* **20**, 11153–11158 (2012).
50. A. N. Kolyadin, A. F. Kosolapov, A. D. Pryamikov, A. S. Biriukov, V. G. Plotnichenko, and E. M. Dianov, "Light transmission in negative curvature hollow core fiber in extremely high material loss region," *Opt. Express* **21**, 9514–9519 (2013).
51. F. Yu and J. C. Knight, "Spectral attenuation limits of silica hollow core negative curvature fiber," *Opt. Express* **21**, 21466–21471 (2013).
52. A. Urich, R. R. J. Maier, F. Yu, J. C. Knight, D. P. Hand, and J. D. Shephard, "Flexible delivery of Er:YAG radiation at 2.94 μm with negative curvature silica

- glass fibers: a new solution for minimally invasive surgical procedures,” *Biomed. Opt. Express* **4**, 193–205 (2013).
53. P. Jaworski, F. Yu, R. R. J. Maier, W. J. Wadsworth, J. C. Knight, J. D. Shephard, and D. P. Hand, “Picosecond and nanosecond pulse delivery through a hollow-core negative curvature fiber for micro-machining applications,” *Opt. Express* **21**, 22742–22753 (2013).
54. A. F. Kosolapov, A. D. Pryamikov, A. S. Biriukov, V. S. Shiryaev, M. S. Astapovich, G. E. Snopatin, V. G. Plotnichenko, M. F. Churbanov, and E. M. Dianov, “Demonstration of CO₂-laser power delivery through chalcogenide-glass fiber with negative-curvature hollow core,” *Opt. Express* **19**, 25723–25728 (2011).
55. B. Debord, A. Amsanpally, M. Chafer, A. Baz, L. Vincetti, J. Blondy, F. Gérôme, and F. Benabid, “7.7 dB/km losses in inhibited coupling hollow-core photonic crystal fibers,” in *Conference on Lasers and Electro-Optics (CLEO)*, OSA Technical Digest (online) (Optical Society of America, 2016), paper JTh4C.8.
56. B. Debord, A. Amsanpally, M. Chafer, A. Baz, M. Maurel, J. M. Blondy, E. Hugonnot, F. Scol, L. Vincetti, F. Gérôme, and F. Benabid, “Ultralow transmission loss in inhibited-coupling guiding hollow fibers,” *Optica* **4**, 209–217 (2017).
57. M. Michieletto, J. K. Lyngs, C. Jakobsen, J. Lgsgaard, O. Bang, and T. T. Alkeskjold, “Hollow-core fibers for high power pulse delivery,” *Opt. Express* **24**, 7103–7119 (2016).
58. J. R. Hayes, S. R. Sandoghchi, T. D. Bradley, Z. Liu, R. Slavik, M. A. Gouveia, N. V. Wheeler, G. T. Jasion, Y. Chen, E. Numkam-Fokoua, M. N. Petrovich, D. J. Richardson, and F. Poletti, “Antiresonant hollow core fiber with octave spanning bandwidth for short haul data communications,” in *Optical Fiber Communication Conference Postdeadline Papers*, OSA Technical Digest (online) (Optical Society of America, 2016), paper Th5A.3.
59. J. R. Hayes, S. R. Sandoghchi, T. D. Bradley, Z. Liu, R. Slavik, M. A. Gouveia, N. V. Wheeler, G. Jasion, Y. Chen, E. N. Fokoua, M. N. Petrovich, D. J. Richardson, and F. Poletti, “Antiresonant hollow core fiber with an octave spanning bandwidth for short haul data communications,” *J. Lightwave Technol.* **35**, 437–442 (2017).
60. N. V. Wheeler, T. D. Bradley, J. R. Hayes, M. A. Gouveia, S. Liang, Y. Chen, S. R. Sandoghchi, S. M. Abokhamis Mousavi, F. Poletti, M. N. Petrovich, and D. J. Richardson, “Low-loss Kagome hollow-core fibers operating from the near-to the mid-IR,” *Opt. Lett.* **42**, 2571–2574 (2017).
61. A. F. Kosolapov, G. K. Alagashev, A. N. Kolyadin, A. D. Pryamikov, A. S. Biryukov, I. A. Bufetov, and E. M. Dianov, “Hollow-core revolver fibre with a double-capillary reflective cladding,” *Quantum Electron.* **46**, 267–270 (2016).
62. C. Wei, R. Kuis, F. Chenard, and J. Hu, “Chalcogenide negative curvature hollow-core photonic crystal fibers with low loss and low power ratio in the glass,” in *Conference on Laser and Electro-Optics (CLEO)*, OSA Technical Digest (online) (Optical Society of America, 2014), paper SM1N.5.
63. W. Belardi and J. C. Knight, “Effect of core boundary curvature on the confinement losses of hollow antiresonant fibers,” *Opt. Express* **21**, 21912–21917 (2013).
64. W. Belardi and J. C. Knight, “Hollow antiresonant fibers with reduced attenuation,” *Opt. Lett.* **39**, 1853–1856 (2014).
65. M. S. Habib, O. Bang, and M. Bache, “Low-loss hollow-core silica fibers with adjacent nested anti-resonant tubes,” *Opt. Express* **23**, 17394–17406 (2015).
66. A. F. Kosolapov, A. Pryamikov, G. Alagashev, A. Kolyadin, A. Biriukov, and E. Dianov, “Negative curvature hollow-core fibers (NCHCFs) for mid-IR applications,” in *Advanced Photonics*, OSA Technical Digest (online) (Optical Society of America, 2014), paper SoTu2B.3.

67. G. K. Alagashev, A. D. Pryamikov, A. F. Kosolapov, A. N. Kolyadin, A. Y. Lukovkin, and A. S. Biriukov, "Impact of geometrical parameters on the optical properties of negative curvature hollow core fibers," *Laser Phys.* **25**, 055101 (2015).
68. W. Belardi and J. C. Knight, "Hollow antiresonant fibers with low bending loss," *Opt. Express* **22**, 10091–10096 (2014).
69. C. Wei, R. A. Kuis, F. Chenard, C. R. Menyuk, and J. Hu, "Higher-order mode suppression in chalcogenide negative curvature fibers," *Opt. Express* **23**, 15824–15832 (2015).
70. C. Wei, O. Alvarez, F. Chenard, and J. Hu, "Empirical glass thickness for chalcogenide negative curvature fibers," in *Summer Topicals Meeting Series* (IEEE Photonics Society, 2015), paper TuE3.3.
71. A. D. Pryamikov, G. K. Alagashev, and A. S. Biriukov, "Impact of core cladding boundary shape on the waveguide properties of hollow core microstructured fibers," *Laser Phys.* **26**, 125104 (2016).
72. J. H. V. Price, T. M. Monro, H. Ebendorff-Heidepriem, F. Poletti, P. Horak, V. Finazzi, J. Y. Y. Leong, P. Petropoulos, J. C. Flanagan, G. Brambilla, X. Feng, and D. J. Richardson, "Mid-IR supercontinuum generation from nonsilica microstructured optical fibers," *IEEE J. Sel. Top. Quantum Electron.* **13**, 738–749 (2007).
73. X. Jiang, N. Y. Joly, M. A. Finger, F. Babic, G. K. L. Wong, J. C. Travers, and P. St.J. Russell, "Deep-ultraviolet to mid-infrared supercontinuum generated in solid-core ZBLAN photonic crystal fibre," *Nat. Photonics* **9**, 133–139 (2015).
74. G. Tao, H. Ebendorff-Heidepriem, A. M. Stolyarov, S. Danto, J. V. Badding, Y. Fink, J. Ballato, and A. F. Abouraddy, "Infrared fibers," *Adv. Opt. Photon.* **7**, 379–458 (2015).
75. W. Belardi, N. White, J. Lousteau, X. Feng, and F. Poletti, "Hollow core anti-resonant fibers in borosilicate glass," in *Workshop on Specialty Optical Fibers and their Applications*, OSA Technical Digest (online) (Optical Society of America, 2015), paper WW4A.4.
76. R. R. Gattass, D. Rhonehouse, D. Gibson, C. C. McClain, R. Thapa, V. Q. Nguyen, S. S. Bayya, R. J. Weiblen, C. R. Menyuk, L. B. Shaw, and J. S. Sanghera, "Infrared glass-based negative-curvature anti-resonant fibers fabricated through extrusion," *Opt. Express* **24**, 25697–25703 (2016).
77. V. S. Shiryaev, "Chalcogenide glass hollow-core microstructured optical fibers," *Front. Mater.* **2**, 24 (2015).
78. V. S. Shiryaev, A. F. Kosolapov, A. D. Pryamikov, G. E. Snopatin, M. F. Churbanov, A. S. Biriukov, T. V. Kotereva, S. V. Mishinov, G. K. Alagashev, and A. N. Kolyadin, "Development of technique for preparation of As₂S₃ glass preforms for hollow core microstructured optical fibers," *J. Optoelectron. Adv. Mater.* **16**, 1020–1025 (2014).
79. P. Uebel, M. C. Günendi, M. H. Frosz, G. Ahmed, N. N. Edavalath, J.-M. Ménard, and P. St.J. Russell, "Broadband robustly single-mode hollow-core PCF by resonant filtering of higher-order modes," *Opt. Lett.* **41**, 1961–1964 (2016).
80. X. Liu, W. Ding, Y. Y. Wang, S. Gao, L. Cao, X. Feng, and P. Wang, "Characterization of a liquid-filled nodeless anti-resonant fiber for biochemical sensing," *Opt. Lett.* **42**, 863–866 (2017).
81. A. V. Newkirk, J. E. Antonio-Lopez, J. Anderson, R. Alvarez-Aguirre, Z. S. Eznavah, G. Lopez-Galmiche, R. Amezcua-Correa, and A. Schülzgen, "Modal analysis of antiresonant hollow core fibers using S² imaging," *Opt. Lett.* **41**, 3277–3280 (2016).

82. V. Setti, L. Vincetti, and A. Argyros, "Flexible tube lattice fibers for terahertz applications," *Opt. Express* **21**, 3388–3399 (2013).
83. Z. Wang, W. Belardi, F. Yu, W. J. Wadsworth, and J. C. Knight, "Efficient diode-pumped mid-infrared emission from acetylene-filled hollow-core fiber," *Opt. Express* **22**, 21872–21878 (2014).
84. W. Belardi, "Design and properties of hollow antiresonant fibers for the visible and near infrared spectral range," *J. Lightwave Technol.* **33**, 4497–4503 (2015).
85. Y. Y. Wang, X. Peng, M. Alharbi, C. F. Dutin, T. D. Bradley, F. Gérôme, M. Mielke, T. Booth, and F. Benabid, "Design and fabrication of hollow-core photonic crystal fibers for high-power ultrashort pulse transportation and pulse compression," *Opt. Lett.* **37**, 3111–3113 (2012).
86. X. Huang, W. Qi, D. Ho, K. T. Yong, F. Luan, and S. Yoo, "Hollow core anti-resonant fiber with split cladding," *Opt. Express* **24**, 7670–7678 (2016).
87. Y. Chen, M. F. Saleh, N. Y. Joly, and F. Biancalana, "Guiding 2.94 μm using low-loss microstructured antiresonant triangular-core fibers," *J. Appl. Phys.* **119**, 143104 (2016).
88. F. Yu, M. Xu, and J. C. Knight, "Experimental study of low-loss single-mode performance in anti-resonant hollow-core fibers," *Opt. Express* **24**, 12969–12975 (2016).
89. W. Ding and Y. Wang, "Analytic model for light guidance in single wall hollow-core anti-resonant fibers," *Opt. Express* **22**, 27242–27256 (2014).
90. X. Liu, Z. Fan, Z. Shi, Y. Ma, J. Yu, and J. Zhang, "Dual-core antiresonant hollow core fibers," *Opt. Express* **24**, 17453–17458 (2016).
91. A. V. V. Nampoothiri, A. M. Jones, C. Fourcade-Dutin, C. Mao, N. Dadashzadeh, B. Baumgart, Y. Y. Wang, M. Alharbi, T. Bradley, N. Campbell, F. Benabid, B. R. Washburn, K. L. Corwin, and W. Rudolph, "Hollow-core optical fiber gas lasers (HOFGLAS): a review [Invited]," *Opt. Mater. Express* **2**, 948–961 (2012).
92. F. Emaury, C. F. Dutin, C. J. Saraceno, M. Trant, O. H. Heckl, Y. Y. Wang, C. Schriber, F. Gerome, T. Südmeyer, F. Benabid, and U. Keller, "Beam delivery and pulse compression to sub-50 fs of a mode locked thin disk laser in a gas-filled Kagome-type HC-PCF fiber," *Opt. Express* **21**, 4986–4994 (2013).
93. A. V. V. Nampoothiri, B. Debord, M. Alharbi, F. Gérôme, F. Benabid, and W. Rudolph, "CW hollow-core optically pumped I_2 fiber gas laser," *Opt. Lett.* **40**, 605–608 (2015).
94. J. Yang, B. Yang, Z. Wang, and W. Liu, "Design of the low-loss wide bandwidth hollow-core terahertz inhibited coupling fibers," *Opt. Commun.* **343**, 150–156 (2015).
95. T. D. Bradley, Y. Wang, M. Alharbi, B. Debord, C. Fourcade-Dutin, B. Beaudou, F. Gerome, and F. Benabid, "Optical properties of low loss (70 dB/km) hypocycloid-core kagome hollow core photonic crystal fiber for Rb and Cs based optical applications," *J. Lightwave Technol.* **31**, 2752–2755 (2013).
96. T. D. Bradley, J. Jouin, J. J. McFerran, P. Thomas, F. Gerome, and F. Benabid, "Extended duration of rubidium vapor in aluminosilicate ceramic coated hypocycloidal core kagome HC-PCF," *J. Lightwave Technol.* **32**, 2486–2491 (2014).
97. L. Vincetti and V. Setti, "Extra loss due to Fano resonances in inhibited coupling fibers based on a lattice of tubes," *Opt. Express* **20**, 14350–14361 (2012).
98. A. Benoît, B. Beaudou, M. Alharbi, B. Debord, F. Gérôme, F. Salin, and F. Benabid, "Over-five octaves wide Raman combs in high-power picosecond-laser pumped H_2 -filled inhibited coupling kagome fiber," *Opt. Express* **23**, 14002–14009 (2015).
99. B. Debord, A. Amsanpally, M. Alharbi, L. Vincetti, J. M. Blondy, F. Gérôme, and F. Benabid, "Ultra-large core size hypocycloid-shape inhibited coupling

- kagome fibers for high-energy laser beam handling,” *J. Lightwave Technol.* **33**, 3630–3634 (2015).
100. X. Zheng, B. Debord, L. Vincetti, B. Beaudou, F. Gérôme, and F. Benabid, “Fusion splice between tapered inhibited coupling hypocycloid-core Kagome fiber and SMF,” *Opt. Express* **24**, 14642–14647 (2016).
 101. D. V. Bogdanovich, A. K. Srivastava, V. G. Chigrinov, A. S. Biriukov, and A. D. Pryamikov, “Hollow core negative curvature fibre with layers of photoaligned optically anisotropic material,” *Laser Phys. Lett.* **12**, 105101 (2015).
 102. A. V. Gladyshev, A. N. Kolyadin, A. F. Kosolapov, Y. P. Yatsenko, A. D. Pryamikov, A. S. Biryukov, I. A. Bufetov, and E. M. Dianov, “Efficient 1.9- μm Raman generation in a hydrogen-filled hollow-core fibre,” *Quantum Electron.* **45**, 807–812 (2015).
 103. A. A. Krylov, A. K. Senatorov, A. D. Pryamikov, A. F. Kosolapov, A. N. Kolyadin, G. K. Alagashev, A. V. Gladyshev, and I. A. Bufetov, “1.56 μm sub-microjoule femtosecond pulse delivery through low-loss microstructured revolver hollow-core fiber,” *Laser Phys. Lett.* **14**, 035104 (2017).
 104. A. D. Pryamikov, A. F. Kosolapov, G. K. Alagashev, A. N. Kolyadin, V. V. Vel'miskin, A. S. Biriukov, and I. A. Bufetov, “Hollow-core microstructured ‘revolver’ fibre for the UV spectral range,” *Quantum Electron.* **46**, 1129–1133 (2016).
 105. Y. P. Yatsenko, E. N. Pleteneva, A. G. Okhrimchuk, A. V. Gladyshev, A. F. Kosolapov, A. N. Kolyadin, and I. A. Bufetov, “Multiband supercontinuum generation in an air-core revolver fibre,” *Quantum Electron.* **47**, 553–560 (2017).
 106. L. Vincetti and V. Setti, “Waveguiding mechanism in tube lattice fibers,” *Opt. Express* **18**, 23133–23146 (2010).
 107. L. Vincetti and V. Setti, “Confinement loss in kagome and tube lattice fibers: comparison and analysis,” *J. Lightwave Technol.* **30**, 1470–1474 (2012).
 108. L. Vincetti, “Single-mode propagation in triangular tube lattice hollow-core terahertz fibers,” *Opt. Commun.* **283**, 979–984 (2010).
 109. W. Lu, S. Lou, and A. Argyros, “Investigation of flexible low-loss hollow-core fibres with tube-lattice cladding for terahertz radiation,” *IEEE J. Sel. Top. Quantum Electron.* **22**, 214–220 (2016).
 110. J. Lu, C. Yu, H. Chang, H. Chen, Y. Li, C. Pan, and C. Sun, “Terahertz air-core microstructure fiber,” *Appl. Phys. Lett.* **92**, 064105 (2008).
 111. L. Vincetti, “Empirical formulas for calculating loss in hollow core tube lattice fibers,” *Opt. Express* **24**, 10313–10325 (2016).
 112. X. Huang, S. Yoo, and K. Yong, “Function of second cladding layer in hollow core tube lattice fibers,” *Sci. Rep.* **7**, 1618 (2017).
 113. A. Hartung, J. Kobelke, A. Schwuchow, K. Wondraczek, J. Bierlich, J. Popp, T. Frosch, and M. A. Schmidt, “Double antiresonant hollow core fiber-guidance in the deep ultraviolet by modified tunneling leaky modes,” *Opt. Express* **22**, 19131–19140 (2014).
 114. A. Hartung, J. Kobelke, A. Schwuchow, K. Wondraczek, J. Bierlich, J. Popp, T. Frosch, and M. A. Schmidt, “Origins of modal loss of antiresonant hollow-core optical fibers in the ultraviolet,” *Opt. Express* **23**, 2557–2565 (2015).
 115. J. R. Hayes, F. Poletti, M. S. Abokhamis, N. V. Wheeler, N. K. Baddela, and D. J. Richardson, “Anti-resonant hexagram hollow core fibers,” *Opt. Express* **23**, 1289–1299 (2015).
 116. A. Hartung, J. Kobelke, A. Schwuchow, J. Bierlich, J. Popp, M. A. Schmidt, and T. Frosch, “Low-loss single-mode guidance in large-core antiresonant hollow-core fibers,” *Opt. Lett.* **40**, 3432–3435 (2015).

117. C. Lai, B. You, J. Lu, T. Lu, J. Peng, C. Sun, and H. Chang, "Modal characteristics of antiresonant reflecting pipe waveguides for terahertz waveguiding," *Opt. Express* **18**, 309–322 (2010).
118. E. Nguema, D. Férachou, G. Humbert, J.-L. Auguste, and J.-M. Blondy, "Broadband terahertz transmission within the air channel of thin-wall pipe," *Opt. Lett.* **36**, 1782–1784 (2011).
119. W. Ding and Y. Wang, "Semi-analytical model for hollow-core anti-resonant fibers," *Front. Phys.* **3**, 16 (2015).
120. J. Hu and C. R. Menyuk, "Understanding leaky modes: slab waveguide revisited," *Adv. Opt. Photon.* **1**, 58–106 (2009).
121. D. Marcuse, *Theory of Dielectric Optical Waveguides*, 2nd ed. (Academic, 1991).
122. M. N. O. Sadiku, *Numerical Techniques in Electromagnetics*, 2nd ed. (CRC Press, 2001).
123. J. Jin, *The Finite Element Method in Electromagnetics*, 2nd ed. (Wiley, 2002).
124. T. P. White, B. T. Kuhlmey, R. C. McPhedran, D. Maystre, G. Renversez, C. M. de Sterke, and L. C. Botten, "Multipole method for microstructured optical fibers. I. Formulation," *J. Opt. Soc. Am. B* **19**, 2322–2330 (2002).
125. J. Hu and C. R. Menyuk, "Leakage loss and bandgap analysis in air-core photonic bandgap fiber for nonsilica glasses," *Opt. Express* **15**, 339–349 (2007).
126. C. Wei, C. R. Menyuk, and J. Hu, "Impact of cladding tubes in chalcogenide negative curvature fibers," *IEEE Photon. J.* **8**, 2200509 (2016).
127. C. Wei, J. Hu, and C. R. Menyuk, "Comparison of loss in silica and chalcogenide negative curvature fibers as the wavelength varies," *Front. Phys.* **4**, 30 (2016).
128. F. Poletti, J. R. Hayes, and D. Richardson, "Optimising the performances of hollow antiresonant fibres," in *37th European Conference and Exposition on Optical Communications*, OSA Technical Digest (CD) (Optical Society of America, 2011), paper Mo.2.LeCervin.2.
129. M. Born and E. Wolf, "Elements of the theory of interference and interferometers," in *Principles of Optics*, 7th ed. (Cambridge University, 1999), pp. 359–366.
130. P. K. Choudhury and T. Yoshino, "A rigorous analysis of the power distribution in plastic clad annular core optical fibers," *Optik* **113**, 481–488 (2002).
131. M. Hautakorpi and M. Kaivola, "Modal analysis of M-type-dielectric-profile optical fibers in the weakly guiding approximation," *J. Opt. Soc. Am. A* **22**, 1163–1169 (2005).
132. B. C. Sarkar, P. K. Choudhury, and T. Yoshino, "On the analysis of a weakly guiding doubly clad dielectric optical fiber with annular core," *Microwave Opt. Technol. Lett.* **31**, 435–439 (2001).
133. Y. Koyamada, "Analysis of core-mode to radiation-mode coupling in fiber Bragg gratings with finite cladding radius," *J. Lightwave Technol.* **18**, 1220–1225 (2000).
134. K. Saitoh and M. Koshiba, "Leakage loss and group velocity dispersion in air-core photonic bandgap fibers," *Opt. Express* **11**, 3100–3109 (2003).
135. C. Wei, C. Menyuk, and J. Hu, "Bending-induced mode non-degeneracy and coupling in chalcogenide negative curvature fibers," *Opt. Express* **24**, 12228–12239 (2016).
136. G. Ren, Z. Wang, S. Lou, and S. Jian, "Mode classification and degeneracy in photonic crystal fibers," *Opt. Express* **11**, 1310–1321 (2003).
137. M. A. Khashan and A. Y. Nassif, "Dispersion of the optical constants of quartz and polymethyl methacrylate glasses in a wide spectral range: 0.2–3 μm ," *Opt. Commun.* **188**, 129–139 (2001).
138. A. Yariv, "Guided wave optics propagation in optical fibers," in *Quantum Electronics*, 3rd ed. (Wiley, 1989), pp. 600–650.

139. B. E. A. Saleh and M. C. Teich, "Guided-wave optics," in *Fundamentals of Photonics*, 2nd ed. (Wiley, 2007), pp. 289–299.
140. K. Saitoh, N. A. Mortensen, and M. Koshiba, "Air-core photonic band-gap fibers: the impact of surface modes," *Opt. Express* **12**, 394–400 (2004).
141. Z. Zhang, Y. Shi, B. Bian, and J. Lu, "Dependence of leaky mode coupling on loss in photonic crystal fiber with hybrid cladding," *Opt. Express* **16**, 1915–1922 (2008).
142. J. Hu and C. R. Menyuk, "Optimization of the operational bandwidth in air-core photonic bandgap fibers for IR transmission," *Opt. Commun.* **282**, 18–21 (2009).
143. K. Saitoh and M. Koshiba, "Confinement losses in air-guiding photonic bandgap fibers," *IEEE Photon. Technol. Lett.* **15**, 236–238 (2003).
144. B. J. Mangan, L. Farr, A. Langford, P. J. Roberts, D. P. Williams, F. Couny, M. Lawman, M. Mason, S. Coupland, R. Flea, H. Sabert, T. A. Birks, J. C. Knight, and P. St.J. Russell, "Low loss (1.7 dB/km) hollow core photonic bandgap fiber," in *Optical Fiber Communication Conference*, OSA Technical Digest (online) (Optical Society of America, 2004), paper PD24.
145. M. H. Frosz, J. Nold, T. Weiss, A. Stefani, F. Babic, S. Rammler, and P. St.J. Russell, "Five-ring hollow-core photonic crystal fiber with 1.8 dB/km loss," *Opt. Lett.* **38**, 2215–2217 (2013).
146. W. Ding and Y. Y. Wang, "Hybrid transmission bands and large birefringence in hollow-core anti-resonant fibers," *Opt. Express* **23**, 21165–21174 (2015).
147. P. Yeh, A. Yariv, and C. Hong, "Electromagnetic propagation in periodic stratified media. I. General theory," *J. Opt. Soc. Am.* **67**, 423–438 (1977).
148. E. N. Fokoua, F. Poletti, and D. J. Richardson, "Analysis of light scattering from surface roughness in hollow-core photonic bandgap fibers," *Opt. Express* **20**, 20980–20991 (2012).
149. W. Belardi and J. C. Knight, "Negative curvature fibers with reduced leakage loss," in *Optical Fiber Communication Conference*, OSA Technical Digest (online) (Optical Society of America, 2014), paper Th2A.45.
150. J. D. Shephard, A. Urich, R. M. Carter, P. Jaworski, R. R. J. Maier, W. Belardi, F. Yu, W. J. Wadsworth, J. C. Knight, and D. P. Hand, "Silica hollow core microstructured fibers for beam delivery in industrial and medical applications," *Front. Phys.* **3**, 24 (2015).
151. M. S. Habib, O. Bang, and M. Bache, "Low-loss single-mode hollow-core fiber with anisotropic anti-resonant elements," *Opt. Express* **24**, 8429–8436 (2016).
152. S. Chaudhuri, L. Van Putten, F. Poletti, and P. Sazio, "Low loss transmission in negative curvature optical fibers with elliptical capillary tubes," *J. Lightwave Technol.* **34**, 4228–4231 (2016).
153. L. D. van Putten, E. N. Fokoua, S. M. A. Mousavi, W. Belardi, S. Chaudhuri, J. V. Badding, and F. Poletti, "Exploring the effect of the core boundary curvature in hollow antiresonant fibers," *IEEE Photon. Technol. Lett.* **29**, 263–266 (2017).
154. M. S. Habib, O. Bang, and M. Bache, "Low-loss hollow-core anti-resonant fibers with semi-circular nested tubes," *IEEE J. Sel. Top. Quantum Electron.* **22**, 4402106 (2016).
155. R. Amezcua-Correa, F. Gérôme, S. G. Leon-Saval, N. G. R. Broderick, T. A. Birks, and J. C. Knight, "Control of surface modes in low loss hollow-core photonic bandgap fibers," *Opt Express* **16**, 1142–1149 (2008).
156. T. Morioka, Y. Awaji, R. Ryf, P. Winzer, D. Richardson, and F. Poletti, "Enhancing optical communications with brand new fibers," *IEEE Commun. Mag.* **50**(2), S31–S42 (2012).
157. J. M. Fini, "Aircore microstructure fibers with suppressed higher-order modes," *Opt. Express* **14**, 11354–11361 (2006).

158. K. Saitoh, N. J. Florous, T. Murao, and M. Koshiba, "Design of photonic band gap fibers with suppressed higher-order modes: towards the development of effectively single mode large hollow-core fiber platforms," *Opt. Express* **14**, 7342–7352 (2006).
159. J. M. Fini, J. W. Nicholson, R. S. Windeler, E. M. Monberg, L. Meng, B. Mangan, A. Desantolo, and F. V. DiMarcello, "Low-loss hollow-core fibers with improved single-modedness," *Opt. Express* **21**, 6233–6242 (2013).
160. T. Murao, K. Saitoh, and M. Koshiba, "Multiple resonant coupling mechanism for suppression of higher-order modes in all-solid photonic bandgap fibers with heterostructured cladding," *Opt. Express* **19**, 1713–1727 (2011).
161. F. Jansen, F. Stutzki, C. Jauregui, J. Limpert, and A. Tünnermann, "Avoided crossings in photonic crystal fibers," *Opt. Express* **19**, 13578–13589 (2011).
162. J. A. West, C. M. Smith, N. F. Borrelli, D. C. Allan, and K. W. Koch, "Surface modes in air-core photonic band-gap fibers," *Opt. Express* **12**, 1485–1496 (2004).
163. C. Wei, C. Menyuk, and J. Hu, "Higher-order mode suppression in chalcogenide negative curvature fibers with gaps between cladding tubes," in *Advanced Photonics 2016 (IPR, NOMA, Sensors, Networks, SPPCom, SOF)*, OSA Technical Digest (online) (Optical Society of America, 2016), paper JT4A.32.
164. F. Meng, B. Liu, Y. Li, C. Wang, and M. Hu, "Low loss hollow-core antiresonant fiber with nested elliptical cladding elements," *IEEE Photon. J.* **9**, 7100211 (2017).
165. M. I. Hasan, N. Akhmediev, and W. Chang, "Positive and negative curvatures nested in an antiresonant hollow-core fiber," *Opt. Lett.* **42**, 703–706 (2017).
166. N. N. Edavalath, M. C. Günendi, R. Beravat, G. K. L. Wong, M. H. Frosz, J.-M. Ménard, and P. St.J. Russell, "Higher-order mode suppression in twisted single-ring hollow-core photonic crystal fibers," *Opt. Lett.* **42**, 2074–2077 (2017).
167. Y. Chen, M. F. Saleh, N. Y. Joly, and F. Biancalana, "Low-loss single-mode negatively curved square-core hollow fibers," *Opt. Lett.* **42**, 1285–1288 (2017).
168. T. D. Bradley, N. V. Wheeler, G. T. Jasion, D. Gray, J. Hayes, M. A. Gouveia, S. R. Sandoghchi, Y. Chen, F. Poletti, D. Richardson, and M. Petrovich, "Modal content in hypocycloid Kagomé hollow core photonic crystal fibers," *Opt. Express* **24**, 15798–15812 (2016).
169. A. V. Newkirk, J. E. Antonio-Lopez, J. Anderson, R. Alvarez-Aguirre, R. Amezcua-Correa, and A. Schulzgen, "Higher order modes in anti-resonant hollow core fibers," in *Advanced Photonics (IPR, NOMA, Sensors, Networks, SPPCom, SOF)*, OSA Technical Digest (online) (Optical Society of America, 2016), paper SoM3F.4.
170. T. Bradley, N. Wheeler, M. Petrovich, G. Jasion, D. Gray, J. Hayes, S. Sandoghchi, Y. Chen, F. Poletti, D. J. Richardson, and M. B. Alonso, "S² measurement of higher order mode content in low loss hypocycloid kagomé hollow core photonic crystal fiber," in *Conference on Lasers and Electro-Optics (CLEO)*, OSA Technical Digest (Optical Society of America, 2016), paper STu4P.8.
171. M. Xu, F. Yu, and J. Knight, "Low-loss anti-resonant hollow-core fibers with single-mode performance," in *Advanced Photonics (IPR, NOMA, Sensors, Networks, SPPCom, SOF)*, OSA Technical Digest (online) (Optical Society of America, 2016), paper SoM3F.5.
172. V. Bock, M. Plötner, O. D. Vries, J. Nold, N. Haarlammert, T. Schreiber, R. Eberhardt, and A. Tünnermann, "Modal content measurements (S²) of negative curvature hollow-core photonic crystal fibers," *Opt. Express* **25**, 3006–3012 (2017).

173. W. Belardi, F. D. Lucia, F. Poletti, and P. J. Sazio, "Composite material hollow antiresonant fibers," *Opt. Lett.* **42**, 2535–2538 (2017).
174. A. D. Pryamikov, A. F. Kosolapov, V. G. Plotnichenko, and E. M. Dianov, "Transmission of CO₂ laser radiation through glass hollow core microstructured fibers," in *CO₂ Laser-Optimisation and Application*, D. C. Dumitras, ed. (InTech, 2012), pp. 227–248.
175. M. H. Frosz, P. Roth, M. C. Günendi, and P. St.J. Russell, "Analytical formulation for the bend loss in single-ring hollow-core photonic crystal fibers," *Photon. Res.* **5**, 88–91 (2017).
176. M. Heiblum and J. H. Harris, "Analysis of curved optical waveguides by conformal transformation," *IEEE J. Quantum Electron.* **11**, 75–83 (1975).
177. J. Hu, C. R. Menyuk, L. B. Shaw, J. S. Sanghera, and I. D. Aggarwal, "Computational study of a 3–5 μm source that is created by using supercontinuum generation in As₂S₃ chalcogenide fibers with a pump at 2 μm," *Opt. Lett.* **35**, 2907–2909 (2010).
178. S. Gao, Y. Wang, X. Liu, W. Ding, and P. Wang, "Bending loss characterization in nodeless hollow-core anti-resonant fiber," *Opt. Express* **24**, 14801–14811 (2016).
179. N. V. Wheeler, A. M. Heidt, N. K. Baddela, E. N. Fokoua, J. R. Hayes, S. R. Sandoghchi, F. Poletti, M. N. Petrovich, and D. J. Richardson, "Low-loss and low-bend-sensitivity mid-infrared guidance in a hollow-core-photonic-bandgap fiber," *Opt. Lett.* **39**, 295–298 (2014).
180. Y. Jung, V. A. J. M. Sleiffer, N. K. Baddela, M. N. Petrovich, J. R. Hayes, N. V. Wheeler, D. R. Gray, E. Numkam Fokoua, J. P. Wooler, H. H.-L. Wong, F. Parmigiani, S.-U. Alam, J. Surof, M. Kuschnerov, V. Veljanovski, H. De Waardt, F. Poletti, and D. J. Richardson, "First demonstration of a broadband 37-cell hollow core photonic bandgap fiber and its application to high capacity mode division multiplexing," in *Optical Fiber Communication Conference/National Fiber Optic Engineers Conference*, OSA Technical Digest (online) (Optical Society of America, 2013), paper PDP5A.3.
181. S. Gao, Y. Wang, X. Liu, W. Ding, and P. Wang, "Optical performance of nodeless hollow-core anti-resonant fiber under bending: the observation of subbands," in *Advanced Photonics (IPR, NOMA, Sensors, Networks, SPCom, SOF)*, OSA Technical Digest (online) (Optical Society of America, 2016), paper SoM3F.6.
182. A. V. V. Nampoothiri, A. Ratanavis, N. Campbell, and W. Rudolph, "Molecular C₂H₂ and HCN lasers pumped by an optical parametric oscillator in the 1.5 μm band," *Opt. Express* **18**, 1946–1951 (2010).
183. J. E. McCord, H. C. Miller, G. Hager, A. I. Lampson, and P. G. Crowell, "Experimental investigation of an optically pumped mid-infrared carbon monoxide laser," *IEEE J. Quantum Electron.* **35**, 1602–1612 (1999).
184. A. M. Jones, A. V. V. Nampoothiri, A. Ratanavis, T. Fiedler, N. V. Wheeler, F. Couny, R. Kadel, F. Benabid, B. R. Washburn, K. L. Corwin, and W. Rudolph, "Mid-infrared gas filled photonic crystal fiber laser based on population inversion," *Opt. Express* **19**, 2309–2316 (2011).
185. M. R. A. Hassan, F. Yu, W. J. Wadsworth, and J. C. Knight, "Cavity-based mid-IR fiber gas laser pumped by a diode laser," *Optica* **3**, 218–221 (2016).
186. S. Wu, C. Wang, C. Fourcade-Dutin, B. R. Washburn, F. Benabid, and K. L. Corwin, "Direct fiber comb stabilization to a gas-filled hollow-core photonic crystal fiber," *Opt. Express* **22**, 23704–23715 (2014).
187. C. M. Harvey, F. Yu, J. C. Knight, W. J. Wadsworth, and P. J. Almeida, "Reduced repetition rate Yb³⁺ mode-locked picosecond fiber laser with hollow core fiber," *IEEE Photon. Technol. Lett.* **28**, 669–672 (2016).

188. B. Debord, M. Alharbi, L. Vincetti, A. Husakou, C. Fourcade-Dutin, C. Hoenninger, E. Mottay, F. Gérôme, and F. Benabid, "Multi-meter fiber-delivery and pulse self-compression of milli-Joule femtosecond laser and fiber-aided laser-micromachining," *Opt. Express* **22**, 10735–10746 (2014).
189. P. Jaworski, F. Yu, R. M. Carter, J. C. Knight, J. D. Shephard, and D. P. Hand, "High energy green nanosecond and picosecond pulse delivery through a negative curvature fiber for precision micro-machining," *Opt. Express* **23**, 8498–8506 (2015).
190. B. Beaudou, F. Gérôme, Y. Y. Wang, M. Alharbi, T. D. Bradley, G. Humbert, J.-L. Auguste, J.-M. Blondy, and F. Benabid, "Millijoule laser pulse delivery for spark ignition through kagome hollow-core fiber," *Opt. Lett.* **37**, 1430–1432 (2012).
191. Y. Wang, M. Alharbi, T. D. Bradley, C. Fourcade-Dutina, B. Deborda, B. Beaudou, F. Gérôme, and F. Benabid, "Hollow-core photonic crystal fibre for high power laser beam delivery," *High Power Laser Sci. Eng.* **1**, 17–28 (2013).
192. T. G. Polanyi, H. C. Bredemeier, and T. W. Davis, Jr., "A CO₂ laser for surgical research," *Med. Biol. Eng.* **8**, 541–548 (1970).
193. K. M. Sasaki, A. Aoki, S. Ichinose, T. Yoshino, S. Yamada, and I. Ishikawa, "Scanning electron microscopy and Fourier transformed infrared spectroscopy analysis of bone removal using Er:YAG and CO₂ lasers," *J. Periodontol.* **73**, 643–652 (2002).
194. S. Amini-Nik, D. Kraemer, M. L. Cowan, K. Gunaratne, P. Nadesan, B. A. Alman, and R. J. D. Miller, "Ultrafast mid-IR laser scalpel: protein signals of the fundamental limits to minimally invasive surgery," *PLoS One* **5**, e13053 (2010).
195. S. Stübinger, B. von Rechenberg, H. F. Zeilhofer, R. Sader, and C. Landes, "Er:YAG laser osteotomy for removal of impacted teeth: clinical comparison of two techniques," *Lasers Surg. Med.* **39**, 583–588 (2007).
196. A. Urich, R. R. J. Maier, F. Yu, J. C. Knight, D. P. Hand, and J. D. Shephard, "Silica hollow core microstructured fibres for mid-infrared surgical applications," *J. Non-Cryst. Solids* **377**, 236–239 (2013).
197. H. Garvie-Cook, "Background," in *Novel (Trans)dermal Drug Delivery Strategies: Micro-and Nano-Scale Assessments* (Springer, 2016), pp. 5–28.
198. H. Garvie-Cook, J. M. Stone, F. Yu, R. H. Guy, and S. N. Gordeev, "Femtosecond pulsed laser ablation to enhance drug delivery across the skin," *J. Biophotonics* **9**, 144–154 (2016).
199. Y. P. Yatsenko, A. A. Krylov, A. D. Pryamikov, A. F. Kosolapov, A. N. Kolyadin, A. V. Gladyshev, and I. A. Bufetov, "Propagation of femtosecond pulses in a hollow-core revolver fibre," *Quantum Electron.* **46**, 617–626 (2016).
200. F. Yu and J. C. Knight, "Negative curvature hollow-core optical fiber," *IEEE J. Sel. Top. Quantum Electron.* **22**, 4400610 (2016).
201. E. M. Dianov, S. L. Semjonov, and I. A. Bufetov, "New generation of optical fibres," *Quantum Electron.* **46**, 1–10 (2016).
202. F. Poletti, N. V. Wheeler, M. N. Petrovich, N. K. Baddela, E. Numkam Fokoua, J. R. Hayes, D. R. Gray, Z. Li, R. Slavik, and D. J. Richardson, "Towards high-capacity fibre-optic communications at the speed of light in vacuum," *Nat. Photonics* **7**, 279–284 (2013).
203. V. A. Sleiffer, Y. Jung, P. Leoni, M. Kushnerov, N. V. Wheeler, N. K. Baddela, R. G. H. van Uden, C. M. Okonkwo, J. R. Hayes, J. Wooler, E. Numkam, R. Slavik, F. Poletti, M. N. Petrovich, V. Veljanovski, S. U. Alam, D. J. Richardson, and H. de Waardt, "30.7 Tb/s (96 × 320 Gb/s) DP-32QAM transmission over 19-cell photonic band gap fiber," in *Optical Fiber Communication*

- Conference/National Fiber Optic Engineers Conference*, OSA Technical Digest (online) (Optical Society of America, 2013), paper OW11.5.
204. C. Dumitrache, J. Rath, and A. P. Yalin, "High power spark delivery system using hollow core kagome lattice fibers," *Materials* **7**, 5700–5710 (2014).
 205. M. R. B. Andreetta, L. S. Cunha, L. F. Vales, L. C. Caraschi, and R. G. Jasinevicius, "Bidimensional codes recorded on an oxide glass surface using a continuous wave CO₂ laser," *J. Micromech. Microeng.* **21**, 025004 (2011).
 206. A. N. Kolyadin, G. K. Alagasheva, A. D. Pryamikova, L. Mouradianb, A. Zeytunyanb, H. Toneyanb, A. F. Kosolapova, and I. A. Bufetov, "Negative curvature hollow-core fibers: dispersion properties and femtosecond pulse delivery," *Phys. Procedia* **73**, 59–66 (2015).
 207. R. M. Carter, W. N. MacPherson, P. Jaworski, F. Yu, R. Beck, J. D. Shephard, and D. P. Hand, "Dispersion measurement of microstructured negative curvature hollow core fiber," *Opt. Eng.* **55**, 116106 (2016).
 208. B. Sherlock, F. Yu, J. Stone, S. Warren, C. Paterson, M. A. A. Neil, P. M. W. French, J. Knight, and C. Dunsby, "Tunable fibre-coupled multiphoton microscopy with a negative curvature fibre," *J. Biophotonics* **9**, 715–720 (2016).
 209. G. I. Stegeman and R. H. Stolen, "Waveguides and fibers for nonlinear optics," *J. Opt. Soc. Am. B* **6**, 652–662 (1989).
 210. J. C. Travers, W. Chang, J. Nold, N. Y. Joly, and P. St.J. Russell, "Ultrafast nonlinear optics in gas-filled hollow-core photonic crystal fibers," *J. Opt. Soc. Am. B* **28**, A11–A26 (2011).
 211. J. M. Dudley and J. R. Taylor, "Ten years of nonlinear optics in photonic crystal fibre," *Nat. Photonics* **3**, 85–90 (2009).
 212. A. R. Bhagwat and A. L. Gaeta, "Nonlinear optics in hollow-core photonic bandgap fibers," *Opt. Express* **16**, 5035–5047 (2008).
 213. P. Hölzer, W. Chang, J. C. Travers, A. Nazarkin, J. Nold, N. Y. Joly, M. Saleh, F. Biancalana, and P. St.J. Russell, "Femtosecond nonlinear fiber optics in the ionization regime," *Phys. Rev. Lett.* **107**, 203901 (2011).
 214. F. Tani, J. C. Travers, and P. St.J. Russell, "Multimode ultrafast nonlinear optics in optical waveguides: numerical modeling and experiments in kagome photonic-crystal fiber," *J. Opt. Soc. Am. B* **31**, 311–320 (2014).
 215. M. I. Hasan, N. Akhmediev, and W. Chang, "Mid-infrared supercontinuum generation in supercritical xenon-filled hollow-core negative curvature fibers," *Opt. Lett.* **41**, 5122–5125 (2016).
 216. M. Cassataro, D. Novoa, M. C. Günendi, N. N. Edavalath, M. H. Frosz, J. C. Travers, and P. St.J. Russell, "Generation of broadband mid-IR and UV light in gas-filled single-ring hollow-core PCF," *Opt. Express* **25**, 7637–7644 (2017).
 217. N. Dadashzadeh, M. P. Thirugnanasambandam, H. W. K. Weerasinghe, B. Debord, M. Chafer, F. Gerome, F. Benabid, B. R. Washburn, and K. L. Corwin, "Near diffraction-limited performance of an OPA pumped acetylene-filled hollow-core fiber laser in the mid-IR," *Opt. Express* **25**, 13351–13358 (2017).
 218. Z. Wang, F. Yu, W. J. Wadsworth, and J. C. Knight, "Efficient 1.9 μm emission in H₂-filled hollow core fiber by pure stimulated vibrational Raman scattering," *Laser Phys. Lett.* **11**, 105807 (2014).
 219. A. N. Kolyadin, G. K. Alagashv, A. D. Pryamikov, A. V. Gladyshev, A. F. Kosolapov, A. S. Biriukov, and I. A. Bufetov, "Negative curvature hollow core fibers for Raman lasing in the mid IR spectral range," *J. Phys.* **737**, 012009 (2016).
 220. Y. Chen, Z. Wang, B. Gu, F. Yu, and Q. Lu, "Achieving a 1.5 μm fiber gas Raman laser source with about 400 kW of peak power and a 6.3 GHz linewidth," *Opt. Lett.* **41**, 5118–5121 (2016).

221. A. V. Gladyshev, A. N. Kolyadin, A. F. Kosolapov, Y. P. Yatsenko, A. D. Pryamikov, A. S. Biriukov, I. A. Bufetov, and E. M. Dianov, "Low-threshold 1.9 μm Raman generation in microstructured hydrogen-filled hollow-core revolver fibre with nested capillaries," *Laser Phys.* **27**, 025101 (2016).
222. B. Gu, Y. Chen, and Z. Wang, "Characteristics of 1.9- μm laser emission from hydrogen-filled hollow-core fiber by vibrational stimulated Raman scattering," *Opt. Eng.* **55**, 126114 (2016).
223. A. V. Gladyshev, A. F. Kosolapov, M. M. Khudyakov, Y. P. Yatsenko, A. N. Kolyadin, A. A. Krylov, A. D. Pryamikov, A. S. Biriukov, M. E. Likhachev, I. A. Bufetov, and E. M. Dianov, "4.4 μm Raman laser based on hollow-core silica fibre," *Quantum Electron.* **47**, 491–494 (2017).
224. B. Debord, M. Alharbi, A. Benoît, D. Ghosh, M. Dontabactouny, L. Vincetti, J.-M. Blondy, F. Gérôme, and F. Benabid, "Ultra low-loss hypocycloid-core Kagome hollow-core photonic crystal fiber for green spectral-range applications," *Opt. Lett.* **39**, 6245–6248 (2014).
225. M. S. Habib, C. Markos, O. Bang, and M. Bache, "Soliton-plasma nonlinear dynamics in mid-IR gas-filled hollow-core fibers," *Opt. Lett.* **42**, 2232–2235 (2017).
226. O. H. Heckl, C. J. Saraceno, C. R. E. Baer, T. Südmeyer, Y. Y. Wang, Y. Cheng, F. Benabid, and U. Keller, "Temporal pulse compression in a xenon-filled Kagome-type hollow-core photonic crystal fiber at high average power," *Opt. Express* **19**, 19142–19149 (2011).
227. F. Emaury, C. J. Saraceno, B. Debord, D. Ghosh, A. Diebold, F. Gérôme, T. Südmeyer, F. Benabid, and U. Keller, "Efficient spectral broadening in the 100-W average power regime using gas-filled kagome HC-PCF and pulse compression," *Opt. Lett.* **39**, 6843–6846 (2014).
228. T. Balciunas, C. Fourcade-Dutin, G. Fan, T. Witting, A. A. Voronin, A. M. Zheltikov, F. Gérôme, G. G. Paulus, A. Baltuska, and F. Benabid, "A strong-field driver in the single-cycle regime based on self-compression in a kagome fibre," *Nat. Commun.* **6**, 6117 (2015).
229. F. Guichard, A. Giree, Y. Zaouter, M. Hanna, G. Machinet, B. Debord, F. Gérôme, P. Dupriez, F. Druon, C. Hönniger, E. Mottay, F. Benabid, and P. Georges, "Nonlinear compression of high energy fiber amplifier pulses in air-filled hypocycloid-core Kagome fiber," *Opt. Express* **23**, 7416–7423 (2015).
230. A. M. Cubillas, X. Jiang, T. G. Euser, N. Taccardi, B. J. M. Etzold, P. Wasserscheid, and P. St.J. Russell, "Photochemistry in a soft-glass single-ring hollow-core photonic crystal fiber," *Analyst* **142**, 925–929 (2017).
231. A. M. Cubillas, S. Unterkofler, T. G. Euser, B. J. Etzold, A. C. Jones, P. J. Sadler, P. Wasserscheid, and P. St.J. Russell, "Photonic crystal fibres for chemical sensing and photochemistry," *Chem. Soc. Rev.* **42**, 8629–8648 (2013).
232. T. Ritari, J. Tuominen, H. Ludvigsen, J. C. Petersen, H. Sorensen, T. P. Hansen, and H. R. Simonsen, "Gas sensing using air-guiding photonic crystal fibers," *Opt. Express* **12**, 4080–4087 (2004).
233. S. Gao, Y. Y. Wang, X. Liu, C. Hong, S. Gu, and P. Wang, "Nodeless hollow-core fiber for the visible spectral range," *Opt. Lett.* **42**, 61–64 (2017).
234. V. Sleiffer, Y. Jung, N. Baddela, J. Surof, M. Kuschnerov, V. Veljanovski, J. Hayes, N. Wheeler, E. Numkam Fokoua, J. Wooler, D. Gray, N. Wong, F. Parmigiani, S. Alam, M. Petrovich, F. Poletti, D. Richardson, and H. de Waardt, "High capacity mode-division multiplexed optical transmission in a novel 37-cell hollow-core photonic bandgap fiber," *J. Lightwave Technol.* **32**, 854–863 (2014).
235. S. Ghosh, J. E. Sharping, D. G. Ouzounov, and A. L. Gaeta, "Resonant optical interactions with molecules confined in photonic band-gap fibers," *Phys. Rev. Lett.* **94**, 093902 (2005).

236. L. W. Kornaszewski, N. Gayraud, J. M. Stone, W. N. Macpherson, A. K. George, J. C. Knight, D. P. Hand, and D. T. Reid, "Mid-infrared methane detection in a photonic bandgap fiber using a broadband optical parametric oscillator," *Opt. Express* **15**, 11219–11224 (2007).
237. N. Gayraud, U. W. Kornaszewski, J. M. Stone, J. C. Knight, D. T. Reid, D. P. Hand, and W. N. MacPherson, "Mid-infrared gas sensing using a photonic bandgap fiber," *Appl. Opt.* **47**, 1269–1277 (2008).
238. A. M. Stolyarov, A. Gumennik, W. McDaniel, O. Shapira, B. Schell, F. Sorin, K. Kuriki, G. Benoit, A. Rose, and J. D. Joannopoulos, "Enhanced chemiluminescent detection scheme for trace vapor sensing in pneumatically-tuned hollow core photonic bandgap fibers," *Opt. Express* **20**, 12407–12415 (2012).
239. W. Liu, T. Guo, A. C. Wong, H. Y. Tam, and S. He, "Highly sensitive bending sensor based on Er³⁺-doped DBR fiber laser," *Opt. Express* **18**, 17834–17840 (2010).
240. M. Deng, C. P. Tang, T. Zhu, and Y. J. Rao, "Highly sensitive bend sensor based on Mach–Zehnder interferometer using photonic crystal fiber," *Opt. Commun.* **284**, 2849–2853 (2011).
241. B. J. Eggleton, B. Luther-Davies, and K. Richardson, "Chalcogenide photonics," *Nat. Photonics* **5**, 141–148 (2011).
242. J. S. Sanghera, L. B. Shaw, and I. D. Aggarwal, "Chalcogenide glass fiber-based mid-IR sources and applications," *IEEE J. Sel. Top. Quantum Electron.* **15**, 114–119 (2009).
243. T. Frosch, M. Schmitt, T. Noll, G. Bringmann, K. Schenzel, and J. Popp, "Ultrasensitive in situ tracing of the alkaloid dioncophylline A in the tropical liana *Triphyophyllum peltatum* by applying deep-UV resonance Raman microscopy," *Anal. Chem.* **79**, 986–993 (2007).
244. T. Frosch, N. Tarcea, M. Schmitt, H. Thiele, F. Langenhorst, and J. Popp, "UV Raman imaging-A promising tool for astrobiology: comparative Raman studies with different excitation wavelengths on SNC Martian meteorites," *Anal. Chem.* **79**, 1101–1108 (2007).
245. E. B. Hanlon, R. Manoharan, T. W. Koo, K. E. Shafer, J. T. Motz, M. Fitzmaurice, J. R. Kramer, I. Itzkan, R. R. Dasari, and M. S. Feld, "Prospects for in vivo Raman spectroscopy," *Phys. Med. Biol.* **45**, R1–R59 (2000).
246. G. J. Leggett, "Light-directed nanosynthesis: near-field optical approaches to integration of the top-down and bottom-up fabrication paradigms," *Nanoscale* **4**, 1840–1855 (2012).
247. L. Vincetti, "Numerical analysis of plastic hollow core microstructured fiber for Terahertz applications," *Opt. Fiber Technol.* **15**, 398–401 (2009).
248. L. Vincetti, V. Setti, and M. Zoboli, "Terahertz tube lattice fibers with octagonal symmetry," *IEEE Photon. Technol. Lett.* **22**, 972–974 (2010).
249. H. Li, G. Ren, B. Zhu, Y. Gao, B. Yin, J. Wang, and S. Jian, "Guiding terahertz orbital angular momentum beams in multimode Kagome hollow-core fibers," *Opt. Lett.* **42**, 179–182 (2017).
250. J. Anthony, R. Leonhardt, S. G. Leon-Saval, and A. Argyros, "THz propagation in kagome hollow-core microstructured fibers," *Opt. Express* **19**, 18470–18478 (2011).
251. A. Dupuis, K. Stoeffler, B. Ung, C. Dubois, and M. Skorobogatiy, "Transmission measurements of hollow-core THz Bragg fibers," *J. Opt. Soc. Am. B* **28**, 896–907 (2011).
252. J. T. Lu, C. H. Lai, T. F. Tseng, H. Chen, Y. F. Tsai, I. J. Chen, Y. J. Hwang, H. C. Chang, and C. K. Sun, "Terahertz polarization-sensitive rectangular pipe waveguides," *Opt. Express* **19**, 21532–21539 (2011).

253. C. S. Ponceca, R. Pobre, E. Estacio, N. Sarukura, A. Argyros, M. C. Large, and M. A. van Eijkelenborg, "Transmission of terahertz radiation using a microstructured polymer optical fiber," *Opt. Lett.* **33**, 902–904 (2008).
254. D. S. Wu, A. Argyros, and S. G. Leon-Saval, "Reducing the size of hollow terahertz waveguides," *J. Lightwave Technol.* **29**, 97–103 (2011).
255. J. Yang, J. Zhao, C. Gong, H. Tian, L. Sun, P. Chen, L. Lin, and W. Liu, "3D printed low-loss THz waveguide based on Kagome photonic crystal structure," *Opt. Express* **24**, 22454–22460 (2016).
256. W. Lu and A. Argyros, "Terahertz spectroscopy and imaging with flexible tube-lattice fiber probe," *J. Lightwave Technol.* **32**, 4621–4627 (2014).
257. S. Atakaramians, A. Stefani, H. Li, M. S. Habib, J. G. Hayashi, A. Tuniz, X. Tang, J. Anthony, R. Lwin, A. Argyros, S. C. Fleming, and B. T. Kuhlmeiy, "Fiber-drawn metamaterial for THz waveguiding and imaging," *J. Infrared Millimeter Terahertz Waves* **38**, 1162–1178 (2017).
258. S. Okaba, T. Takano, F. Benabid, T. Bradley, L. Vincetti, Z. Maizelis, V. Yampol'skii, F. Nori, and H. Katori, "Lamb-Dicke spectroscopy of atoms in a hollow-core photonic crystal fibre," *Nat. Commun.* **5**, 4096 (2014).
259. L. Vincetti and V. Setti, "Elliptical hollow core tube lattice fibers for terahertz applications," *Opt. Fiber Technol.* **19**, 31–34 (2013).
260. S. A. Mousavi, D. J. Richardson, S. R. Sandoghchi, and F. Poletti, "First design of high birefringence and polarising hollow core anti-resonant fibre," in *European Conference on Optical Communication (ECOC)*, Valencia (2015), pp. 1–3.
261. S. A. Mousavi, S. R. Sandoghchi, D. J. Richardson, and F. Poletti, "Broadband high birefringence and polarizing hollow core antiresonant fibers," *Opt. Express* **24**, 22943–22958 (2016).
262. M. J. Li, J. A. West, and K. W. Koch, "Modeling effects of structural distortions on air-core photonic bandgap fibers," *J. Lightwave Technol.* **25**, 2463–2468 (2007).
263. E. N. Fokoua, D. J. Richardson, and F. Poletti, "Impact of structural distortions on the performance of hollow-core photonic bandgap fibers," *Opt. Express* **22**, 2735–2744 (2014).
264. E. N. Fokoua, S. R. Sandoghchi, Y. Chen, G. T. Jasion, N. V. Wheeler, N. K. Baddela, J. R. Hayes, M. N. Petrovich, D. J. Richardson, and F. Poletti, "Accurate modelling of fabricated hollow-core photonic bandgap fibers," *Opt. Express* **23**, 23117–23132 (2015).
265. R. J. Weiblen, C. R. Menyuk, R. R. Gattass, L. B. Shaw, and J. S. Sanghera, "Fabrication tolerances in As₂S₃ negative-curvature antiresonant fibers," *Opt. Lett.* **41**, 2624–2627 (2016).
266. W. J. Wadsworth, F. Yu, and J. C. Knight, "Useful light from photonic crystal fibres," in *Conference on Lasers and Electro-Optics (CLEO)*, OSA Technical Digest (Optical Society of America, 2016), paper SW11.5. (Mentioned in the talk).



Chengli Wei is a Ph.D. candidate in the Department of Electrical and Computer Engineering at Baylor University. He received his B.S. degree from Tianjin University and his M.S. degree from Nankai University in China. Currently, he is working as a research assistant in the Photonics Research Lab directed by Dr. Jonathan Hu. His research interests include negative curvature fibers, chalcogenide glass fibers, photonic crystal fibers, nonlinear fiber optics, nanophotonics, and surface plasmons. He is a member of

the Optical Society of America and the IEEE Photonics Society.



R. Joseph Weiblen received his B.S. degree in Computer Engineering from the University of Maryland, Baltimore County in 2007 and his Ph.D. degree in Electrical Engineering from UMBC in 2015. He is currently a postdoctoral fellow at the Naval Research Laboratory in Washington, DC. His doctoral research was on mid-infrared fiber optics, including novel chalcogenide waveguides, supercontinuum generation, and nanostructured antireflective coatings. His research interests include mid-infrared fiber optics, nanostructured antireflective coatings, antiresonant fibers, microresonator-based optical frequency combs, and optical metamaterials. Dr. Weiblen is a member of the Optical Society of America and the IEEE Photonics Society.



Curtis R. Menyuk was born March 26, 1954. He received B.S. and M.S. degrees from MIT in 1976 and his Ph.D. from UCLA in 1981. He has worked as a research associate at the University of Maryland, College Park and at Science Applications International Corporation in McLean, Virginia. In 1986 he became an Associate Professor in the Department of Electrical Engineering at the University of Maryland Baltimore County, and he was the founding member of this department. In 1993, he was promoted to Professor. He was on partial leave from UMBC from fall 1996 until fall 2002. From 1996–2001, he worked part-time for the Department of Defense, co-directing the Optical Networking program at the DoD Laboratory for Telecommunications Sciences in Adelphi, Maryland from 1999–2001. In 2001–2002, he was Chief Scientist at PhotonEx Corporation. In 2008–2009, he was a JILA Visiting Fellow at the University of Colorado. For the last 30 years, his primary research area has been theoretical and computational studies of lasers, nonlinear optics, and fiber optic communications. He has authored or co-authored more than 270 archival journal publications as well as numerous other publications and presentations, and he is a co-inventor of five patents. He has also edited three books. The equations and algorithms that he and his research group at UMBC have developed to model optical fiber systems are used extensively in the telecommunications and photonics industry. He is a member of the Society for Industrial and Applied Mathematics and of SPIE. He is a fellow of the American Physical Society, the Optical Society of America, and the IEEE. He is the 1996–1999 UMBC Presidential Research Professor, the winner of the 2013 IEEE Photonics Society William Streifer Award, and a 2015–2016 winner of the Humboldt Foundation Research Award.



Jonathan Hu is an Associate Professor in the Department of Electrical and Computer Engineering at Baylor University. He received his Ph.D. degree from the University of Maryland, Baltimore County. Before he joined Baylor University in August 2011, he spent two years as a Research Associate at Princeton University. His research interests include mid-IR supercontinuum generation, chalcogenide glass fibers, photonic crystal fibers, optical amplifiers, nonlinear optics, nanophotonics, 2D materials, and surface plasmons. He has authored or co-authored over 60 refereed journal and conference publications. In 2015, he served as a topic co-chair for Mid Infrared Photonics (MIP) in the IEEE Summer Topical Meetings. He received Baylor ECS Research Initiation Award in 2014 and Baylor Young Investigator Development Award in 2015.